LBL-11842
Preprint

Lawrence Berkeley Laboratory
UNIVERSITY OF CALIFORNIA

Materials & Molecular
Research Division

To be published in the Proceedings of the Royal Society of London

THE RESPONSE OF SOLIDS TO ELASTIC/PLASTIC INDENTATION

S.S. Chiang, D.B. Marshall, and A.G. Evans

November 1980

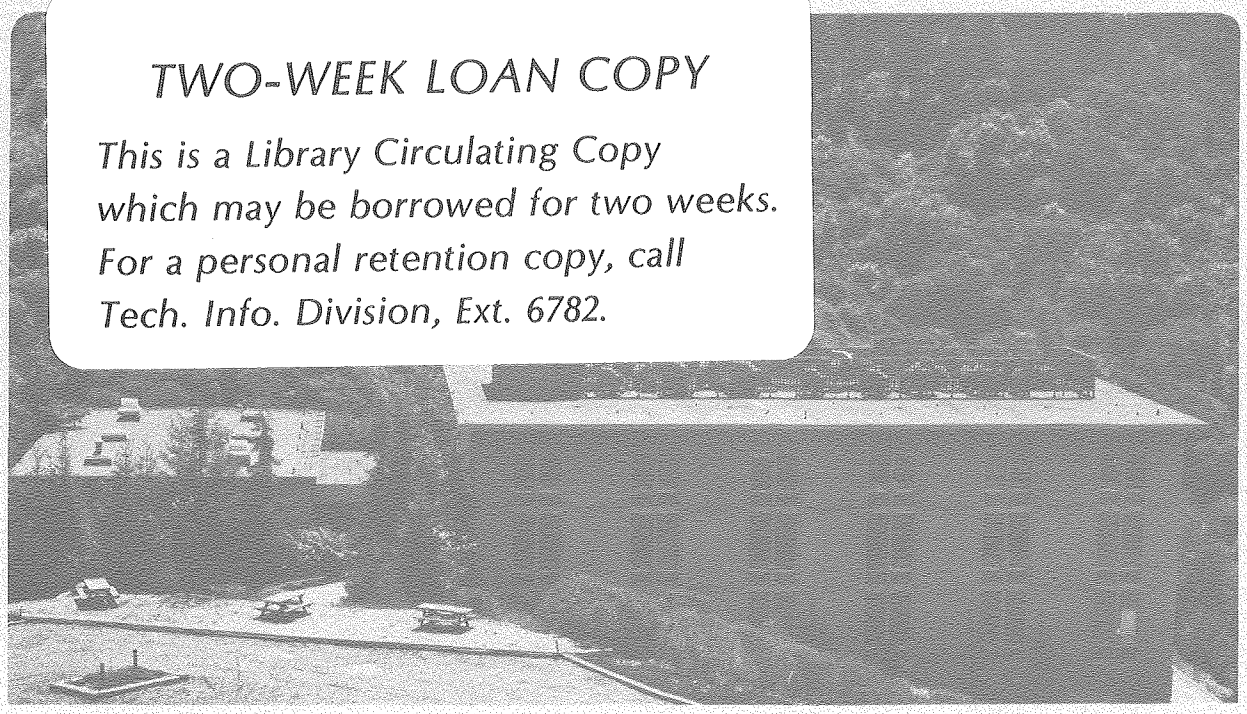

Prepared for the U.S. Department of Energy under Contract W-7405-ENG-48

DISCLAIMER

THE RESPONSE OF SOLIDS TO ELASTIC/PLASTIC INDENTATION

S.S. Chiang, D.B. Marshall and A.G. Evans

Materials and Molecular Research Division, Lawrence Berkeley Laboratory
and Department of Materials Science and Mineral Engineering,
University of California, Berkeley, California 94720

ABSTRACT

A new approach for analysing indentation plasticity and indentation fracture is presented. The analysis permits relations to be established between material properties (notably hardness, yield strength and elastic modulus) and the dimensions of the indentation and plastic zone. The predictions are demonstrated to be fully consistent with observations performed on a wide range of materials. The indentation stress fields can also be adapted to generate predictions of indentation fracture thresholds for the three dominant crack types: radial, median and lateral cracks. The predictions are generally consistent with experimental observations.

This manuscript was printed from originals provided by the authors.

1. INTRODUCTION

The response of solids to indentation provides information of central interest to such important phenomena as erosion (Wiederhorn and Ruff 1979, Evans 1979a), wear (Koepke 1979, Evans 1979b), machining damage (Marshall, Lawn and Mecholsky 1980) and (surface-controlled) fracture strength (Marshall and Lawn 1979a). This association is particularly strong in brittle materials for which indentation fracture dictates the material degradation process. Considerable progress toward describing "well-developed" indentation fracture, for a given material/indenter system, has been achieved by adopting scaling arguments (Lawn and Fuller 1975; Marshall and Lawn 1979b; Lawn, Evans and Marshall 1980) or semi-empirical dimensional analyses (Evans and Wilshaw 1976); procedures which avert the requirement for a complete description of the elastic/plastic indentation. However, the crack iniation threshold and the trends in the fracture behavior with material properties (effects which are sensitive to the details of indentation response) have not been adequately addressed. The extent of plasticity, the magnitude of the elastic/plastic stress field and their dependence upon material properties, such as hardness and elastic modulus (Lawn and Evans 1976; Lawn, Evans and Marshall 1980), are issues of primary importance to these aspects of the indentation fracture problem. This paper provides a self-consistent analysis pertinent to these effects.

Observations of indentation plasticity by Samuels and Mulhearn (1957) and by Mulhearn (1959) have revealed two fundamentally different modes of deformation response. For (equivalent) conical indenters with small included anges a cutting process, with a plastic zone shape that accords with rigid/plastic (e.g. slip-line field) expectations, is observed. For

indenters of large included angle,the plastic zone shows spherical symmetry (usually hemispherical), even in materials subject to ready plasticity (e.g. annealed brass). This deformation response (referred to as radial compression) exhibits analogies with the elastic/plastic deformation expected around a cavity subject to internal pressure (Hill 1950). The difference between the two deformation responses to indentation is also manifest in the degree of material pile-up around the indentation. In the rigid/plastic regime material is displaced to the surface and therefore gives rise to a large raised lip around the indentation; whereas, for radial compression, very little pile-up is observed. The transition appears to occur over a range of cone angles (Mulhearn 1959; Atkins and Tabor 1965), such that lower transition angles pertain to materials with a higher hardness-to-modulus ratio. For example, the transition range is $\sim$120° for aluminum (Haddow and Johnson 1961), $\sim$105° for work-hardened mild steel (Atkins and Tabor 1965) and $\sim$60° for cold rolled brass (Mulhearn 1959). An interpretation of the behavior of indentations exhibited hemispherical plasticity is the primary focus of this paper.

The analogy between the hemispherical indentation zone and the pressurized spherical cavity has been recognized previously, but not fully exploited. Dugdale (1958) and Mulhearn (1959) used a rigid-plastic, radial-compression model to relate hardness to the stress strain curve and to calculate the plastic strain field. Marsh (1964) derived a semi-empirical relation between indentation pressure (hardness) and the ratio of elastic modulus to yield stress, based on Hill's (1950) spherical cavity expansion solution for infinite elastic/plastic materials. The reduced constraint around the hemsipherical cavity was introduced by allowing two constants

to be adjusted to fit experimental measurements. However, effects of indenter geometry were not explicitly considered. In an alternative analysis, which has been widely adopted in recent studies of indentation, Johnson (1970) attempted to account for the influence of indenter angle by allowing the indentation pressure to be transmitted via an incompressible hydrostatic core beneath the indenter. However, the core in this analysis is a nebulous entity and the predicted indentation pressures appreciably underestimate the measured values (see figures 2 and 3).

The present approach commences by reassessing the correlation between indentation deformation and the spherical cavity model, and then develops new concepts for extending the spherical cavity solution to account for the reduced half-space constraint. The approach suggests an analytic procedure for calculating the stress field around an indentation. The stresses deduced in accord with this procedure will be used to consolidate further the indentation plasticity problem and thus to permit trends in the indentation pressure and plastic zone radius (with yield stress and elastic modulus) to be predicted and compared with the experiment. In addition, the stress analysis permits trends in the fracture initiation threshold with material properties to be derived and correlated with experimental observations. Finally, some implications for fracture propagation behavior also emerge from the analysis.

2. INDENTATION ANALYSES

2.1 Basic Hypotheses

Two hypotheses establish the present basis for relating indentation deformation to the spherical cavity model. Firstly, the extent of

plasticity (as manifest in the volume V of the plastic zone) is considered to be fundamentally dictated by the plastic work of indentation. Secondly, the plastic zone volume is assumed to be related exclusively to the indentation volume ΔV, independent of the indenter geometry. This proposal is based on observations (and numerical calculations) of spherical symmetry in the plastic zone, regardless of indenter geometry [Samuels and Mulhearn (1957); Mulhearn (1959); Swain (1978); Evans, Gulden and Rosenblatt (1978); Burlingame (1980)] and, in particular, the observation of identical plastic zone boundaries for spherical and Vickers pyramidal indentations of equal volume (Samuels and Mulhearn, 1957).

The above hypotheses necessarily require that the indentation pressure be independent of indenter geometry, because the plastic work of indentation is the product of the indentation pressure and the volume of indentation. The experimental results of Atkins and Tabor (1965) on steel and copper are in reasonable accord with this requirement. Specifically, the hardness was determined to vary by <10% over the range of cone angles for which deformation occurs by radial compression (the actual variation depends on the degree of prior work hardening of the indented material; constant hardness occurs at a work hardening strain of about 0.1 - 0.2). In Section 2.2 the results of pyramidal indentations performed in soda-lime glass, ZnS and As_2S_3 glass are presented to confirm the approximate shape independence of the indentation pressure and plastic zone volume.

The assumed shape invariance of the indentation pressure and plastic zone dimension permits experimental indentation results to be referred to a common indentation geometry. A convenient reference geometry is the hemispherical indentation, radius a, with hemispherical plastic zone, radius b.

The relative hemispherical indentation dimensions, β , can then be simply expressed by the relation

$$\beta = b/a = (V/\Delta V)^{1/3} \tag{1a}$$

which for pyramidal indentation becomes

$$b/a = (b/\bar{a})\ (\pi/\cot\Psi)^{1/3} \tag{1b}$$

where $2\bar{a}$ is the identation diagonal and 2Ψ is the included angle betweeen opposite edges of the pyramid†. Transferring the indentation pressure directly to the reference geometry permits experimental results to be readily compared with hemispherical indentation analyses. The detailed comparison will be conducted following the stress analysis of the elastic/plastic indentation. However, preliminary credence in the hypotheses is established later in this section by demonstrating a reasonably close correlation between experimental results and the expectations of the spherical cavity solution.

2.2 Effect of Indenter Geometry on Indentation Pressure

The hypotheses of the previous section were examined by conducting hardness measurements on several brittle materials, using a wide range of indenter geometries. Pyramidal indenters with included angles of 60°, 90°, 120°, 140° and 160° were constructed from a sapphire rod and mounted in a standard microhardness machine. The pyramidal geometry was chosen because the hardness measurement is not significantly affected by the elastic recovery that occurs during unloading (Marsh 1964), even for materials of low modulus to hardness ratio. The test materials, soda lime glass, zinc

†For a Vickers indenter, $\Psi = 74°$, and $a = 0.45\bar{a}$,

sulphide and As_2S_3 glass, were selected to afford a wide range of hardness-to modulus ratio, while maintaining a low absolute hardness with respect to the sapphire indenters.

The results are shown in figure 1, where the indentation pressure (load divided by projected indentation area) is plotted against indenter angle. Also included are measurements obtained from a standard diamond Vickers indenter. The variation of indentation pressure is less than 10% over the entire range of indenters. This compares with a variation of a factor of ten in the indentation volume (at constant load) between the 60° and 160° indenters. Additionally, comparison of the results from the diamond and sapphire indenters, as shown in fig. 1, indicates that the measured indentation pressures are influenced neither by the indenter material nor by frictional effects† between the indenter and test piece.

2.3 Correlation Between Indentation Experiments and the Spherical Cavity Solution

A preliminary analysis of indentation plasticity is conducted, in accord with the above hypotheses, by adopting the results of the spherical cavity solution (Hill 1950);

$$\frac{p}{Y} = \frac{2}{3}\left[1 + \ell n\ (\beta)^3\right] \tag{2a}$$

$$\frac{E}{Y} = 3\ (1-\nu)(\beta)^3 - 2(1-2\nu) \tag{2b}$$

where p is the indentation pressure, Y is the yield stress, E is Young's modulus, ν is Poisson's ratio and β is defined in eqn.(1).

†The sapphire payramids were not as perfectly polished as the commercial Vickers pyramid and would therefore be expected to show larger frictional effects.

These relations can be rearranged to yield expressions that are suitable for direct comparison with experimental results;

$$\frac{E}{P} = \frac{9\,[(1-\nu)\,(\beta)^3 - 2(1-2\nu)/3]}{2[1 + \ell n(\beta)^3]} \tag{3a}$$

$$\frac{p}{Y} = \frac{2}{3}\left\{1 + \ell n\left[\frac{(E/Y) + 2(1-2\nu)}{3(1-\nu)}\right]\right\} \tag{3b}$$

These expressions are plotted in figs. 2, 3. The experimental and numerical results for the relative plastic zone size β, (table I) are compared with equation (3a) in fig. 2. The quality of the correlation (which has not previously been attempted) is encouraging. In particular, it is noted that the experimental results imply that a smaller indentation pressure is needed to attain equivalent plastic zone dimensions in the half-space: a tendency consistent with the reduced elastic constraint of the half-space. This trend is ultimately quantified in section 3.2.1.

Experimental results relating indentation pressure, yield stress and elastic modulus, elicited from the studies of Marsh (1964) and Hirst and Howse (1969) are compared with equation (3b) in fig. 3. (The results for the polymers are given different symbols because these materials are subject in part to densification plasticity during indentation - as manifest in a refractive index change in the plastic zone (Puttick, 1978) - and may not, therefore, be suitable for comparison with elastic/plastic solutions). Again, there is both a good correlation and a tendency for the experimental results to deviate appropriately, toward lower indentation pressures. The existence of this correlation could, in fact, have been deduced from Marsh's interpretation of trends in the indentation pressure,

in which a reduced constraint was implicitly included in the derivation of a semi-empirical relation for the indentation pressure. The role of the reduced constraint is quantified in section 3.2.1.

It is appropriate at this juncture to compare the above correlation with that achieved by Johnson (figs. 2, 3). It is noted that the comparison is less satisfactory, particularly with regard to the plastic zone dimension.

3. STRESS ANALYSIS

3.1 The Method of Solution

Previous studies of elastic/plastic indentation stress fields include an analytic solution (Perrott, 1977) and several numerical solutions (Hardy et al 1971, Evans 1979c). The analytic solution is based on the premise that the stresses within the elastic zone are identical in form to the stress field created by fully-elastic indentation. This is not an acceptable assumption for the (axisymmetric) indentation problem† and hence, the solution yields stress fields that are inconsistent with several observed trends in crack evolution and in indentation plasticity. The numerical solutions are limited in scope, and do not provide a sufficient characterization of the indentation stress field to permit further analysis. (However, the results provide invaluable sources of comparison, at coincidence points, with analytic solutions). The stress fields needed for the analysis of trends in both fracture thresholds and indentation plasticity are developed in the present paper, using boundary conditions suggested by the reference

† Elastic stress fields under elastic/plastic conditions are only necessarily similar in form to the equivalent elastic field when the problem is fully symmetric (e.g., in the pressurized spherical cavity). More generally, the only requirement imposed by the elastic solution is that St. Venant's principle be satisfied i.e., that the far field stresses be equivalent to those given by the elastic-solution (the Boussinesq solution in this case).

hemispherical indentation[†], discussed in section 2.

The approach commences with the elastic/plastic solution for a spherical cavity, radius a, under a pressure p, which creates a spherical plastic zone, radius b. This provides an initially symmetric elastic/plastic field (fig. 4). Then a free surface is created by eliminating the tangential stress field acting over a plane through the cavity center (fig. 4). This is achieved by using the elastic point force solutions pertinent to the half-plane problem provided by Mindlin (1936), i.e. point forces that do not create either a normal stress or in-plane shear stresses at the 'surface' plane. The stresses that result from these forces superimpose onto the initial, symmetric stresses to generate the indentation stress field. This procedure would not normally be justified for elastic/plastic problems. However, it will be demonstrated that, for the present problem, this approach (by virtue of the symmetry) provides a self-consistent solution.

Application of the surface forces induces a radial stress, σ_r^s, at the location of the cavity interface (fig. 4). For calculations of the stress field while the pressure is still being applied, the effect of the stress σ_r^s is to create a modified pressure p' ($p' = p - \sigma_r^s$). This modified pressure pertains to the selected plastic zone and cavity dimensions, and thereby becomes that indentation pressure (or hardness, H) associated with a plastic zone of relative size β. All stresses should thus be referred to the pressure p'.

For calculations of the residual stress field, it is not permissable to retain a stress at the cavity surface. Hence, in this instance, the

---

† Small deviations from hemispherical symmetry occur in the immediate vicinity of the free surface; but these deviations reduce in magnitude as the penetration increases: becoming negligible at penetrations of one diameter.

stress is eliminated by an iterative scheme, involving the sequential application of cavity surface pressure and point forces until the residual forces become negligibly small.

The application of surface forces along a plane bisecting the cavity must also generate shear stresses within the half plane, which will superimpose upon the shear stresses provided by the symmetrical cavity solution (fig. 4). However, within the plastic zone, the maximum principal shear stress is required to be uniform in order to satisfy the Tresca criterion. It is implicit in the calculation, therefore, that the body forces result in a constant principal shear stress within this zone. Additional shear stress of significant magnitude would superimpose on those provided by the symmetrical solution; in essence, changing the yield strength of the material, from Y to Y'. The effective yield strength of a material with a relative indentation plastic zone dimension β thus becomes Y'.

The rationale for expecting the Mindlin forces to provide a relatively uniform shear stress in the plastic zone is based upon the observed spherical symmetry of the plastic boundary. The premise must be justified, however, by the results of the calculations. Specifically, the calculations must indicate spherically symmetric contours of constant shear stress within the plastic zone. It will be demonstrated that these requirements are reasonably well satisfied. Hence, the method of calculation satisfies both boundary conditions: viz., a stress-free surface and an approximately uniform shear stress within the plastic zone. A self-consistent solution can thus be obtained using the proposed approach.

The stress field solutions obtained in the above manner can only be strictly applicable to a hemispherical indentation. The influence of the

indenter geometry, although a minor perturbation upon the residual stress field (because the indentation surface is stress free and significant geometric effects would only be manifest in the immediate vicinity of the indentation), can be appreciable at peak load. The origin of the peak load geometry effect is associated with the shape independence of the hardness. As the shape changes (at constant indentation volume) the applied force must also change in order to maintain a constant hardness (fig. 4). Hence, it is immediately evident that the remote elastic field must change in accord with St. Venant's principle. Presumably, a near field shape dependence can also be expected. It is expedient, therefore, to calculate bounds on the peak load stress field. One bound is provided by the hemispherical cavity solution. The other is given by superimposing onto the residual field the stress field for a half space subject to a force acting at the indentation center (fig. 4). The magnitude of the force is selected to coincide with that pertinent to the Vickers indenter.

3.2 The Indentation Stress Field

The general form of the stress analysis provides a basis for examining those specific features that relate to the hardness, yield strength, and the incidence of fracture. The two constituents of the indentation stress field are the initial field, provided by the cavity expansion solution, and the free surface modification.

The radial σ_r and tangential σ_t stresses within the initial field (Hill 1950) are given, during load application by;

$$\left.\begin{aligned}
\frac{\sigma_r^{p\ell}}{p} &= \left[\frac{3\ell n\ (r/a)}{1 + 3\ell n(\beta)}\right] - 1 \\
\frac{\sigma_t^{p\ell}}{p} &= \frac{3[\ell n(r/a) + 1/2]}{1 + 3\ell n\beta} - 1
\end{aligned}\right\} \quad (\beta > r/a > 1)$$

$$\left.\begin{aligned}
\frac{\sigma_r^{e\ell}}{p} &= \frac{-\beta^3}{(r/a)^3(1 + 3\ell n\beta)} \\
\frac{\sigma_t^{e\ell}}{p} &= \frac{\beta^3}{2(r/a)^3(1 + 3\ell n\beta)}
\end{aligned}\right\} \quad (r/a > \beta) \qquad (4)$$

where the superscripts $p\ell$ and $e\ell$ indicate the plastic and elastic regions respectively and r is distance from the cavity center. The equivalent stresses after load removal are;

$$\left.\begin{aligned}
\frac{\sigma_r^{rp\ell}}{p} &= \left[\frac{3\ell n\ (r/a)}{1 + 3\ell n\beta}\right] - 1 + \frac{1}{(r/a)^3} \\
\frac{\sigma_t^{rp\ell}}{p} &= \frac{3[\ell n(r/a) + 1/2]}{1 + 3\ell n\beta} - 1 - \frac{1}{2(r/a)^3}
\end{aligned}\right\} \quad (\beta > r/a > 1)$$

$$\left.\begin{aligned}
\frac{\sigma_r^{re\ell}}{p} &= \frac{1}{(r/a)^3}\left[1 - \frac{\beta^3}{1 + 3\ell n\beta}\right] \\
\frac{\sigma_t^{re\ell}}{p} &= \frac{1}{2(r/a)^3}\left[\frac{\beta^3}{1 + 3\ell n\beta} - 1\right]
\end{aligned}\right\} \quad (r/a > \beta) \qquad (5)$$

where σ^r refers to the residual field.

The stresses σ^s created by the surface forces have the general form;

$$\frac{\sigma^s_{mm}}{p} = \int_{plastic} dA \; \frac{\sigma^j_t}{p} \; g_{mm} + \int_{elastic} dA \; \frac{\sigma^k_t}{p} \; g_{mm} \qquad (6)$$

where $j = p\ell$, $k = e\ell$ at peak load, and $j = rp\ell$, $k = re\ell$ for the residual field, $mm = xx$, xz or zz, (the stress distribution in cartesian coordinates) or r, t, ϕ, (in spherical coordinates) and g_{mm} are the point force functions summarized in the Appendix. The final stresses are obtained by the superposition of eqn. (6) and eqn. (4) or (5).

The stresses at the peak load condition deduced by this procedure represent an upper bound. Lower peak bound load stresses can be obtained by superimposing onto the residual field the stresses that derive from a point force applied at the center of the indentation.

$$\frac{\sigma_{mm}}{p} = 2(\bar{a})^2 g_{mm} \qquad (7)$$

3.2.1. The Modified Pressure and Yield Strength

The radial and tangential stresses induced within the plastic zone by the surface forces result in a pressure modification, which establishes the hardness H of the material, and in a shear stress modification, which dictates the effective yield strength, Y'. The stresses that effect these modifications are σ^s_r and σ^s_ϕ which are given by eqn. (6), evaluated at peak load condition, with $mm = r$ or ϕ.

Taking $\nu = 0.25$, the variations of H/p along the cavity interface are plotted in fig. 5 for several values of β. The relative uniformity of H/p for each β indicates that the requisite constant pressure boundary condition along the indentation interface is satisfied. The indentation pressure can now be directly related to the cavity pressure p, by

superposition†;

$$H/p = 1 - \sigma_r^s/p \equiv 1 - m \tag{8}$$

The effective yield strength of the material at any location in the plastic zone is given by;

$$Y' = Y + (\sigma_\phi^s - \sigma_r^s) \tag{9a}$$

or, expressed in normalised form;

$$\frac{Y'}{H} = \frac{(Y/p) + \sigma_\phi^s/p - \sigma_r^s/p}{1 - \sigma_r^s/p} \tag{9b}$$

where σ_ϕ is that component of the tangential stress normal to the angle ϕ (fig. 4). The yield strengths at the indentation interface and at the elastic/plastic boundary are plotted for several β in fig. 6. It is noted that reasonable uniformity of Y' is retained around each of these contours; although significant fluctuations begin to develop at the larger values of β. Within the uncertainty associated with these fluctuations, the magnitude of Y' is essentially the same at the elastic/plastic boundary and at the indentation interface; and similar to the original value of the yield strength, Y. No significant change in the yield strength can thus be attributed to the creation of the free surface. This relative maintenance of yield strength uniformity probably accounts for the observed hemispherical symmetry of the plastic zone.

The modified ratio of indentation pressure to yield strength thus

†When the specimen is fully unloaded, σ_r^s and m are replaced by σ_r^{rs} and m_r respectively. The variations of m and m_r with β are plotted in fig. 7.

becomes H/Y, and replaces p/Y for all subsequent analyses. The lower indentation pressure reflects the reduction in constraint induced by the free surface, as anticipated from the indentation plasticity measurements (figs. 2, 3). The modified pressure can be used to reevaluate the relationship between the indentation characteristics, H and β, and the elastic and plastic properties, E and Y, of the material. These revised curves are plotted on figs. 2 and 3. A good correlation with the experimental results is apparent. Some justification for the free surface modification deduced by the present analysis is thus established. It is also noted that the present analysis has, for the first time, permitted consistent relationships to be established between all of the indentation variables: the pressure, yield strength, elastic modulus and plastic zone dimensions.

3.2.2. The Stress Field

The general form of the stress field is axisymmetric, but relatively complex. The results presented in this section thus emphasize only the components of the stress field and the spatial locations that relate to the formation of the three dominant crack systems: radial cracking (dictated by the σ_{yy} stress near the free surface and the elastic/plastic boundary), median cracking (dictated by the σ_{yy} stress near the base of the plastic zone), and lateral fracture (dominated by the σ_{zz} stress in the same general vicinity). The stresses are deduced from the general equations (as detailed in the Appendix) both at peak load and in the fully unloaded conditions, for several values of β.

a. The Radial System

The constituents of the surface tangential stresses, σ_{yy}, derived

from the original spherical cavity solution and the modifications afforded by the surface forces are compared in fig. 8. It is observed that the modification becomes more dominant as the relative plastic zone size β increases. Also, as expected, the modified stress becomes negligible remote from the plastic zone. However, the most significant influence of the modification is the enhancement of the peak tension at the elastic/plastic boundary. Also plotted in fig. 8 are the stresses created by a point force located at the indentation center, used as a constituent of the lower bound stress at peak load. This illustrates both the compressive character of the stresses and their appreciable magnitude in the vicinity of the elastic/plastic boundary (especially for the small plastic zone dimension).

The trends in the resultant stress with β are illustrated in fig. 9. The peak value of the realtive stress σ_{yy}/H diminishes slightly as β increases, whereas the scale of the stress field exhibits a substantial increase. The residual tensile stresses are generally just in excess of the upper bound tensions, at the peak load. However, the equivalent lower bound solution indicates that the tensile stresses at the peak load are appreciably suppressed by indenters with shallow cone angles (particularly for materials with small relative plastic zone dimensions).

The gradient of stress from the surface into the interior of the specimens is also of substantial interest[†]. The stress, plotted in fig. 10, is observed to decrease quite rapidly with distance from the surface, particularly for small β.

[†]The surface stress is subject to error when determined by numerical integration. However, the level of the surface stress needed to obtain an accurate assessment of the stress gradient can be determined analytically, as detailed in the Appendix.

b. The Median System

The trends in the σ_{yy} stress pertinent to median fracture (fig. 11) are similar to those obtained for the radial fracture problem. But, in this instance, the peak load tensile stresses exceed the residual stresses. Also the peak load stresses are found to be relatively insensitive to the indenter geometry and hence, only the lower bound solution is plotted. Note that the peak values of the tension are appreciably smaller than the equivalent tangential tensile stresses near the surface. The stress decreases with distance from the axis (fig. 12), but the gradient is relatively small, especially for larger values of β .

c. The Lateral System

The magnitudes of the σ_{zz} stresses at various axial locations are plotted in fig. 13 for $\beta = 2.2$. It is apparent that the maxium tensions occur at a distance beneath the surface of $\sim\beta/2$. The trends in the stress with β along the planes of maximum tension are illustrated in fig. 14. Again a decrease in the relative peak tension with increases in β is evident. However, in this case, the residual tension is appreciably larger than the upper bound tension at the peak load, indicating a greater tendency for the development of tension during unloading than encountered with the radial system.

4. INDENTATION FRACTURE

4.1. Crack Propagation

The extension of well developed radial/median cracks has been examined in detail in a recent analysis, based upon the magnitude of the effective residual 'force' exerted by the plastic zone on the surrounding elastic material (Lawn, Evans and Marshall, 1980). This analysis yields a relation

for the crack length that depends upon the relative magnitude β of the plastic zone. The original choice of β was a tentative one based on Hill's spherical cavity solution, $\beta \sim (E/H)^{1/2}$, and gave a crack length relation

$$\frac{K_c}{H\sqrt{\bar{a}}}\left(\frac{E}{H}\right)^{1/2} = 0.028\ (\bar{a}/c)^{3/2} \qquad (10)$$

where the numerical quantity is calibrated from experimental results on glass. A more pertinent relation between β and material properties can be derived from the correlation presented in figure 2. Using $\beta \sim (E/H)^{2/5}$ appropriate to this figure, equation (10) becomes

$$\frac{K_c}{H\sqrt{\bar{a}}}\left(\frac{H}{E}\right)^{3/5} = 0.021\ (\bar{a}/c)^{3/2} \qquad (11)$$

The data from Lawn, Evans and Marshall are plotted according to equation (11) in figure 15. This plot shows an improved correlation, thus futher substantiating the merits of this approach for establishing the extension of well developed radial cracks.

4.2 Fracture Initiation

a. Observations

The fracture initiation process at indentations is subject to appreciable complexity. The intitiation sequence frequently involves two stages; nucleation of small microcracks, followed by the extension of those microcracks suitably located in the general indentation stress field (Evans and Wilshaw, 1976, Lawn and Evans 1977). The nucleation stage may involve microcracking of regions of large localized stress concentration; microcracks have been identified at grain boundaries in polycrystals (presumably at dislocation

pile-ups), at slip band intersections in single crystals, and at shear band intersections in glasses (Hagan, 1979). Alternatively, pre-existing microcracks may serve as suitable crack nuclei. However the nucleation phase is not expected to be the critical phase, because non-propagating microcracks are usually observed. The significant step in fracture initiation is thus considered to be the activation of the microcracks by the general indentation field (Lawn and Evans, 1977).

The activation of microcracks by the indentation field is necessarily statistical in nature (particularly if pre-existing microcracks act as nuclei). However it has been noted that the characteristic behavior of cracks within stress fields of rapid spatial variation (typical of indentation) permits the definition of an absolute fracture initiation minimum (Lawn and Evans 1977). Indentation fracture thresholds must exceed the absolute minimum, P_{min} , by an amount that depends on the probabilistic consideration of microcrack location, size and orientation; large numbers of indentations would allow the lowest initiation load to approach P_{min} . The minimum threshold is therefore a useful parameter for establishing initiation trends in processes that involve multiple indentations (e.g. erosion, abrasive wear, machining damage).

The minimum force required to initiate cracks has been studied for a range of materials (Table III, Lankford and Davidson, 1979). Acoustic emission measurements performed during indentation, coupled with direct observations after indentation (using a Vickers Pyramid) suggested that radial cracks were the first to initiate, and that initiation occurred during loading. Direct observations during indentation of soda-lime glass (using

an inverted optical microscope and dry nitrogen environment (Marshall and Lawn, 1979b) also indicated that the minimum threshold pertained to radial crack nucleation, but the cracks formed while unloading (Table III). Since radial cracks always appear to exhibit the lowest threshold, pre-existing surface cracks may be an important source of nuclei. This possibility is investigated in more detail later in this section.

b. Analysis

The prediction of the minimum threshold involves the systematic estimation of stress intensity factors for cracks of various profiles, centered at different locations, in order to obtain the shape and location that yields the maximum peak value for K. Such a systematic study has not yet been conducted. Instead, it is firstly assumed that a crack centered on the elastic/plastic boundary will experience the largest K, because this is the contour of maximum tension within the indentation field. Then, for simplicity, the crack is considered to exhibit circular symmetry, as suggested by the crack profiles observed after initiation. Thereafter, the stress intensity factors can be deduced from the stress field by a superposition method. The stress fields of the pertinent locations for median, radial and lateral fracture initiation are not generally axisymmetric, so the computed stress intensity factors would vary around the crack front. A convenient simplification that yields a uniform crack front K is adopted. This averts appreciable calculational complexity without detracting significantly from the prediction of behavioral trends. The procedure consists of the determination of an effective axisymmetric stress σ_{eff} at each radial location, assumed to be equal to the stress (at that location) averaged over

the full angular range, 0 to 2π. The stress intensity factor can then be derived from the superposition solution;

$$K = 2\left(\frac{c}{\pi}\right)^{1/2}\int_0^1 \frac{\sigma_{eff}(r/c)d(r/c)}{\sqrt{1-(r/c)^2}} \qquad (12)$$

The effective stress normalized by the hardness, can be adequately represented by a polynomial

$$\sigma_{eff}/H = a_o - a_1(r/a) + a_2(r/a)^2 + \ldots\ldots \qquad (13)$$

where the parameters a_o , a_1 (both positive) and a_2 (either positive or negative) are dependent on the relative plastic zone size β . Insertion of equation (13) into equation (12), followed by integration yields the result

$$K/H\,a^{1/2} = f(\delta) = 2(\delta/\pi)^{1/2}[a_o - (\pi a_1/4)\delta + (2a_2/3)\delta^2 + \ldots.] \qquad (14)$$

where $\delta = c/a$. This relation exhibits a peak in the stress intensity factor (when $dK/dc = 0$). This peak coincides with a <u>specific</u> relative crack length, given by (neglecting coefficients a_n , with $n>3$)

$$\delta^* = (3/80a_2)\left[3\pi a_1 - \sqrt{9\pi^2 a_1^2 - 640\, a_o a_2/3}\right] \qquad (15)$$

A minimum threshold occurs when the peak value of K attains K_c . The crack length at the minimum threshold is

$$c^* = \delta^*\, a_{min} = \delta^*[K_{IC}/H\, f(\delta^*)]^2 \qquad (16)$$

and the threshold load for a Vickers pyramidal indenter becomes

$$P_{min} = 2H\,\bar{a}^2_{min} = 2H[K_{IC}/H\,f(\delta^*)]^4/(0.45)^2 \qquad (17)$$

The results summarized in equations (16) and (17) reduce to the Lawn and Evans (1977) result when a_2 is set to zero*. The trends in the threshold with material toughness and hardness are thus essentially the same as those elucidated in the earlier study, except that an additional influence of E/H emerges through the influence of the relative plastic zone size β. This additional influence is illustrated in figure 16. It is noted that the minimum normalized threshold load decreases as β increases, causing a relative diminution of the threshold as the extent of plasticity increases.

The minimum threshold loads for the three crack types (radial, median, lateral), predicted for materials with a range of β values, are shown in Table II. The calculations are referred to the Vickers geometry. Radial cracks exhibit the lowest thresholds and lateral cracks the largest. The median cracks invariably exhibit their lower threshold during loading; while the lateral crack threshold always prevails during the unloading cycle. The occurrence of the radial crack threshold depends upon the indentation geometry. For those configurations best described by the upper bound stress field, the threshold could occur during loading or unloading, by virtue of the similarity in the threshold condition. However, shallow indentation geometries, which are best represented by the lower bound stress, favor radial crack formation during unloading.

---

*The other difference between the Lawn and Evans study and the present analysis is that the former used only order-of-magnitude estimates of a_0 and a_1.

Observed radial crack threshold conditions are compared with predictions in Table III. Good agreement is shown for Ge, Si, Al_2O_3 and ZnS. The observed threshold for NaCl appears to be lower than predicted. However, as noted by Lankford and Davidson , the NaCl threshold is sensitive to crystallographic orientation; the experimental value listed in Table II corresponds to cracks parallel to <110>. Radial cracks could not be nucleated in other orientations, within the available load range (∿60N). The <110> cracks in NaCl (and other ionic solids) are coincident with the primary slip bands that occur outside the generalised plastic zone. The cracks result from an enhancement of the local stress by the stress field of the dislocations, and a threshold appreciably smaller than that associated with the generalised deformation is to be anticipated.

The observed thresholds for glass are an order of magnitude higher than predicted. This observation suggests that the precursor flaw density is too small to permit an appreciable sampling of flaws of the requisite size, at the minimum threshold load. Elevation of the observed threshold above the absolute minimum is not generally observed and hence, its occurrence in glass requires an explanation. A plausible interpretation emerges when the radial crack precursors are considered to be pre-existent surface located microcracks. Then, surfaces prepared by mechanical procedures are likely to exhibit high density of surface cracks and the absolute minimum threshold should be closely approached. This condition pertains for the tests performed on Si, Ge, ZnS and Al_2O_3. However, for surfaces prepared without deliberate mechanical interaction (such as glass surfaces) appreciably lower surface crack densities might be expected, and some elevation above

absolute minimum might be anticipated. The excess threshold load can be quantified (in terms of the availability of pre-existing nucleating flaws) by adapting some existing statistical data for surface flaws in glass (Matthews, McClintock and Shack 1976). The statistical analysis firstly invokes the characteristic variation in stress intensity factor with crack length in order to determine the pre-existing crack radius c_i (fig. 17). Inspection of the trends in stress intensity factor indicates a rapid increase on K at small flaw lengths (up to the maximum). Relatively small deviations of the pre-existing flaw size below c^* would thus substantially elevate the observed threshold, in qualitative accord with the observation for glass. The radius of the pre-existing radial crack nucleus, c_i, can be directly deduced from the K curve by superimposing the ratio of the measured final radial crack length, c_f, and the indentation diagonal, $2\bar{a}_f$, as indicated on fig. 17. The flaw radius pertinent to samples tested in air (c_f = 17μm at $\bar{a}_f$ = 10μm) is determined to be c_i = 0.5μm, i.e. $\sim c^*/2$ The probability of locating flaws of this magnitude within the indentation field at the threshold load can now be estimated from the surface flaw density data. The flaw density data are described in terms of the quantity $g(S)dS$, which is the number of surface flaws in unit area with a strength between S and $S + dS$. An approximate linear fit to the density function gives;

$$\log[g(s)] = 2.9(S/S_{max}) - 2.4 \qquad (18)$$

where $S_{max} = 8.7 \times 10^8$Pa. The number of surface flaws with a strength S existing in an area ΔA $(\Delta A = \pi(r_2^2 - r_1^2))$ is thus;

$$G(S) = \Delta A \int_0^S g(S)\, dS \tag{19}$$

The strength of a surface flaw is related to its radius by;

$$S = \frac{\sqrt{\pi}}{2.5} \frac{K_c}{\sqrt{c}} \tag{20}$$

The number of flaws with radius $\geq c$ in the area A is thus

$$G(c) = \Delta A \int_0^{0.71\frac{K_c}{\sqrt{c}}} g(S)dS \tag{21}$$

At the observed threshold load (5N) the area of surface subject to significant residual tension is $3 \times 10^{-9} m^2$ †. The expected number of flaws in the tensile zone (at initiation) with a size >0.5μm thus becomes ∿0.1. This is sufficiently close to the required value of unity (considering the approximate nature of the flaw statistics, the tensile area sampled and the unknown relative influences of subcritical crack growth in the air environment) that the statistical description is considered to provide a reasonable interpretative description of the excess threshold load.

Finally the predicted radial crack thresholds for some polycrystalline materials are shown in Table IV. It is noted that, because the threshold crack dimension for most of the materials is approximately equal to, or smaller than, the grain size, single crystal material properties (H, E and K_c) would normally provide a more appropriate basis for prediction. The sensitivity to the choice of material parameters is illustrated by comparing the predictions for Al_2O_3 in Table III (based on single crystal material properties) and Table IV (based on polycrystal material properties). The

†The area is estimated by taking $r_1 = 2a$ and $r_2 = 4a$.

prediction in Table IV represents an order-of-magnitude overestimate of the observed threshold. A similar overestimate is apparently obtained for SiC, since the predictions in Table IV exceed the experimental measurements (Lankford and Davidson) by a factor of $\sim$10 ($p^* = 0.1$, $c^* = 1.0\mu m$). Suitable single crystal material parameters are not available for SiC. Hence, a more pertinent prediction of the threshold cannot be performed at the juncture.

5. CONCLUSIONS

Indentation plasticity has been examined by adapting the notions that the volume of the plastic zone and the work of plastic penetration are both dictated by indentation volume. The indentation problem can then be solved by reference to a common hemispherical indentation geometry. This geometry is related to the pressurized cavity problem solved by Hill, modified to account for the reduced constraint in the presence of the free surface. A simple hemispherical modification of the Hill solution has been developed which indicates the essential relationships between indentation plasticity and the dominant material properties: notably, yield strength, hardness, elastic modulus and Poisson's ratio. Predictions of the plastic zone dimension in terms of the hardness and elastic modulus have been shown to correlate with experimental observations for a wide range of materials. Similarly, predictions of the trend in the yield strength/hardness ratio with the elastic modulus and hardness correspond closely to the trends demonstrated by the available experimental data.

The concept has been used to calculate the tensile stress fields generated around indentations, as a basis for predicting the initiation of indentation fractures. The presence of the free surface allows tensile stresses to be developed, during loading or while unloading, that are

qualitatively consistent with observations of the three principal crack types: radial, median and lateral. The stress fields have been used to predict fracture initiation thresholds for the three crack systems. The radial cracks were anticipated to exhibit the lowest threshold loads, as observed experimentally. Comparison of the predicted radial crack threshold loads with experimental results indicate satisfactory correlations for surfaces containing a sufficient density of pre-existent crack initiation sites. This condition was not satisfied for glass surfaces and the experimentally observed threshold was appreciably in excess of the prediction. The excess threshold was rationalized by invoking the weakest link flaw statistics concepts, using data obtained for comparable glass surfaces.

ACKNOWLEDGMENTS

This work was supported by the Division of Materials Sciences, Office of Basic Energy Sciences, U.S. Department of Energy under contract No. W-7405-Eng-48.

APPENDIX

DETAILED EXPRESSIONS FOR INDENTATION STRESS FIELD DETERMINATION

I. The Point Force Solution

A semi-infinite elastic homogeneous solid is considered to be bounded by the plane $z = 0$, the positive z axis penetrating into the body. For a point force p applied at point $(0,0,0)$ and acting in the positive z direction, the stress at a point (x,y,z) inside the semi-infinite body has been determined by Mindlin (1936). The solutions are;

$$\sigma_{xx} = pg_{xx}$$

$$\sigma_{yy} = pg_{yy}$$

$$\sigma_{zz} = pg_{zz}$$

$$\sigma_{xz} = pg_{xz}$$

where

$$g_{xx} = \frac{z}{2\pi R^3}\left[1 - 2\nu - 3\left(\frac{x}{R}\right)^2 - \frac{1-2\nu}{(R+z)^2}\left(R^2 - x^2 + \frac{R}{z}(R^2-2x^2)\right)\right]$$

$$g_{yy} = \frac{z}{2\pi R^3}\left[1 - 2\nu - 3\left(\frac{y}{R}\right)^2 - \frac{1-2\nu}{(R+z)^2}\left(R^2 - y^2 + \frac{R}{z}(R^2-2y^2)\right)\right]$$

$$g_{zz} = -3z^3/2\pi R^5$$

$$g_{xz} = -3xz^2/2\pi R^5$$

here $R^2 = x^2 + y^2 + z^2$ and ν is Poisson's ratio.

In terms of spherical coordinates (r,t,ϕ), the stress at a point $(x,0,z)$ in the x-z plane is:

$$g_r = g_{xx}\cos^2\phi + g_{zz}\sin^2\phi + 2g_{xz}\sin\phi\cos\phi$$

$$g_t = g_{xx}\sin^2\phi + g_{zz}\cos^2\phi + 2g_{xz}\sin\phi\cos\phi$$

$$g_\phi = g_{yy}$$

II. The Stress Relations For The Three Crack Systems

1. The Radial System

The components of the σ_{yy} stress, along the surface ($\zeta=0$) pertinent to radial fracture, are given at peak load, for the upper bound, by* ($\zeta=0$);

$$\frac{\sigma_{yy}^{p\ell}}{H} = \frac{1}{(1-m)}\left[\frac{3\ell n\Omega + 3/2}{1+3\ell n\beta} - 1\right]$$

$$\frac{\sigma_{yy}^{e\ell}}{H} = \frac{1}{(1-m)}\left[\frac{\beta^3}{2\Omega^3(1+3\ell n\beta)}\right] \qquad \text{(A-1)}$$

where $\Omega = x/a$

$$\frac{\sigma_{yy}^{s}}{H} = \frac{2}{(1-m)}\int_1^\beta\int_0^\pi a^2\xi d\xi d\theta\left(\frac{\sigma_t^{p\ell}}{p}\right)g_{yy} + \int_\beta^\infty\int_0^\pi a^2\xi d\xi d\theta\left(\frac{\sigma_t^{e\ell}}{p}\right)g_{yy}$$

(A-2)

*The greek letters represent distances normalized with respect to the cavity radius a (fig. 18).

where

$$g_{yy} = \frac{\zeta}{2\pi a^2 \gamma^3}\left[1 - 2\nu - 3\left(\frac{\eta}{\gamma}\right)^2 - \frac{1-2\nu}{(\gamma+\zeta)^2}\left(\gamma^2 - \eta^2 + \frac{\gamma}{\zeta}(\gamma^2 - 2\eta^2)\right)\right]$$

$$\eta = \xi\sin\theta$$

$$\gamma^2 = \xi^2 + \Omega^2 + \zeta^2 - 2\xi\Omega\cos\theta$$

At peak load, for the lower bound;

$$\frac{\sigma_{yy}^{s}}{H} = \frac{-(1-2\nu)}{(1-m)\Omega^2}$$

At full unload (ζ=0)

$$\frac{\sigma_{yy}^{rp\ell}}{H} = \frac{1}{(1-m)}\left[\frac{3\ell n\Omega + 3/2}{1+3\ell n\beta} - 1 - \frac{(1-2m_r)}{2\Omega^3}\right]$$

$$\frac{\sigma_{yy}^{re\ell}}{H} = \left[\frac{1}{2(1-m)\Omega^3}\quad\frac{\beta^3}{1+3\ell n\beta} - 1 + m_r\right] \qquad \text{(A-3)}$$

where m_r is the term that permits creation of a stress free indentation surface (fig. 7) as obtained by an iteration technique.

2. The Median System

The components of the σ_{yy} stress pertinent to the median fracture problem are not very different from the σ_{yy} stress relevant to radial fracture. At peak load $\sigma_{yy}^{p\ell}/H$ and $\sigma_{yy}^{e\ell}/H$ bear the same form as eqn. (A-1), except that Ω is replaced by ζ (the median crack propagates

along the plane $\Omega = 0$), and σ_{yy}^{s}/H is the same as eqn. (A-2), except that γ^2 becomes, $\gamma^2 = \xi^2 + \zeta^2$. At full unload, the same change should be made, i.e. Ω replaced by ζ, in equation (A-3).

3. The Lateral System

The components of the σ_{zz} stress that pertain to the lateral fracture problem are, at peak load, for the upper bound;

$$\frac{\sigma_{zz}^{p\ell}}{H} = \frac{1}{(1-m)}\left[\frac{3\ell n(\Omega^2+\zeta^2)}{2(1+3\ell n\beta)} + \frac{3\Omega^2}{2(1+3\ell n\beta)(\Omega^2+\zeta^2)} - 1\right]$$

$$\frac{\sigma_{zz}^{e\ell}}{H} = \frac{1}{(1-m)}\left[\frac{\beta^3}{(\Omega^2+\zeta^2)^{5/2}(1+3\ell n\beta)}\ (\Omega^2/2 - \zeta^2)\right] \qquad \text{(A-4)}$$

σ_{zz}^{s}/H exhibits the same form as eqn. (A-2) except that g_{yy} is replaced by g_{zz}, where $g_{zz} = -3\zeta^3/2\pi a^2\gamma^5$ and $\zeta = z/a$.

At peak load, for the lower bound,

$$\frac{\sigma_{zz}^{s}}{H} = -\frac{3\zeta^3}{(1-m)(\Omega^2+\zeta^2)^{5/2}} \qquad \text{(A-5)}$$

At full unload

$$\frac{\sigma_{zz}^{rp\ell}}{H} = \frac{1}{(1-m)}\left[\frac{3\ell n(\Omega^2+\zeta^2)}{2(1+3\ell n\beta)} + \frac{3\Omega^2}{2(1+3\ell n\beta)(\zeta^2+\Omega^2)} + \frac{(\zeta^2-\Omega^2/2)}{(\zeta^2+\Omega^2)}(1-m_r) - 1\right]$$

$$\frac{\sigma_{zz}^{re\ell}}{H} = \frac{1}{(1-m)}\left[1 - m_r - \frac{\beta^3}{1+3\ell n\beta}\right]\ \frac{(\zeta^2 - \Omega^2/2)}{(\zeta^2+\Omega^2)^{5/2}} \qquad \text{(A-6)}$$

III. Analytic Solution For The Surface Stresses

At full load, the modification to the tangential stress on the surface (responsible for radial cracking) created by the free surface is;

$$\frac{\sigma_{yy}^{s}}{H} = \frac{2}{(1-m)}\left[\int_{1}^{\beta}\int_{0}^{\pi} a^2\xi d\xi d\theta \;\frac{\sigma_t^{p\ell}}{H}\,(g_{yy}) + \int_{\beta}^{\infty}\int_{0}^{\pi} a^2\xi d\xi d\theta \;\frac{\sigma_t^{e\ell}}{H}\,(g_{yy})\right] \tag{A-7}$$

When $\zeta = 0$,

$$g_{yy} = -\frac{(1-2\nu)}{2\pi\gamma^4 a^2}\left[\xi^2 + \Omega^2 - 2\xi\Omega\cos\theta - 2\xi^2\sin^2\theta\right] \tag{A-8}$$

Substituting eqn. (A-8) into eqn. (A-7) the stress becomes

$$\frac{\sigma_{yy}^{s}}{H} = \frac{(1-2\nu)}{\pi(1-m)}\left[\int_{1}^{\beta}(-A)\;\frac{\sigma_t^{p\ell}}{H}\;\xi d\xi + \int_{\beta}^{\infty}(-A)\;\frac{\sigma_t^{e\ell}}{H}\;\xi d\xi\right] \tag{A-9}$$

where

$$A = \int_{0}^{\pi}\frac{\xi^2 + \Omega^2 - 2\xi\Omega\cos\theta - 2\xi^2\sin^2\theta}{(\xi^2 + \Omega^2 - 2\xi\Omega\cos\theta)^2}\,d\theta$$

$$= \begin{cases} \dfrac{\pi}{\Omega^2} & \left(\Omega^2 > \xi^2\right) \\ 0 & \left(\xi^2 > \Omega^2\right) \end{cases}$$

if $\Omega < \beta$

$$\frac{\sigma_{yy}^{s}}{H} = \frac{(1-2\nu)}{(1-m)\Omega^2}\left\{\frac{3}{1+3\ell n\beta}\left[\Omega\ell n\Omega - (1/2)(\Omega-1)\right] - (\Omega-1)\right\} \tag{A-10}$$

if $\Omega > \beta$

$$\frac{\sigma_{yy}^{s}}{H} = \frac{(1-2\nu)}{(1-m)\Omega^2}\left\{\frac{1}{1+3\ell n\beta}\left[3\beta\ell n\beta - 1/2\beta + 3/2 - \frac{\beta^3}{4\Omega^2}\right] - (\beta-1)\right\} \quad \text{(A-11)}$$

At full unload, if $\Omega < \beta$

$$\frac{\sigma_{yy}^{s}}{H} = \frac{(1-2\nu)}{(1-m)\Omega^2}\left\{\frac{3}{1+3\ell n\beta}\left[\Omega\ell n\Omega - (1/2)(\Omega-1)\right] + \frac{1-m_r}{4}\left(\frac{1}{\Omega^2} - 1\right)\right\} \quad \text{(A-12)}$$

if $\Omega > \beta$

$$\frac{\sigma_{yy}^{s}}{H} = \frac{(1-2\nu)}{(1-m)\Omega^2}\left\{\frac{1}{1+3\ell n\beta}\left[3\beta\ell n\beta - 1/2\beta + 3/2 - \frac{\beta^3}{4\Omega^2}\right] - (\beta-1) - (1-m_r)\left(\frac{1}{\Omega^2}-1\right)\right\} \quad \text{(A-13)}$$

REFERENCES

Atkins, A.G and Tabor, D. (1965), J. Mech. Phys. Solids, 13, 149-164.

Burlingame, N. H. (1980), M.S. Thesis, University of California, Berkeley.

Dugdale, D. S. (1958), J. Mech. Phys. Solids, 6, 85-91

Evans, A. G. (1979a), "Treatise on Materials Science and Technology, Vol. 16, Erosion," Academic Press, 1-67.

Evans, A. G. (1979b), "Science of Ceramic Machining and Surface Finishing, II," NBS Special Technical Publication: 562, p. 75-92.

Evans, A. G. (1979c),"Fracture Mechanics Applied to Brittle Materials," ASTM STP 678, 112-135.

Evans, A. G. and Wilshaw, T. R. (1976), Acta Metall., 24, 939-956.

Evans, A. G., Gulden, M. E., and Rosenblatt, M. E. (1978), Proc. Roy. Soc., A361, 343-365.

Freiman, S. W., Mckinney, K. R., and Smith, H. L. (1978) in Fracture Mechanics of Ceramics (Eds. Bradt, R. C., Hasselman, D. P. H., and Lange, F. F.), Plenum Press, New York, 657-676.

Haddow, I. B., and Johnson, W. (1961), Int. J. Mech. Sci., 3, 229.

Hagan, J. T. (1979), J. Mat. Sci. 14, 462-466.

Hagan, J. T., and Swain, M. V. (1978), J. Phys. D: Appl. Phys. 11, 2091-2102.

Hardy, C., Baronet, C. H., and Tordion, G. V. (1971), Int'l Jnl. Num. Methds. Eng., 3, 451-462.

Hill, R. (1950), "The Mathematical Theory of Plasticity," Oxford: Clarendon Press.

Hirst, W. and Howse, M. G. J. (1969), Proc. Roy. Soc. A311, 429-444.

Jaccodine, R. J. (1963), J. Electrochem. Soc., 6, 524-527.

Johnson, K. L. (1970), J. Mech. Phys. Solids, 18, 115-126.

Koepke, B. G. and Stokes, R. J. (1979), Science of Machining and Surface Finishing II, NBS Special Technical Publication: 562, p. 75-92.

Lankford, J. and Davidson, D. L. (1979), J. Mater. Sci., 14, 1662-1668.

Lawn, B. R. and Fuller, E. R. (1975), J. Mater. Sci., 10, 2016-2024.

Lawn, B. R. and Wilshaw, T. R. (1975) "Fracture of Brittle Solids," Cambridge University Press.

Lawn, B. R., and Evans, A. G. (1977), J. Mater. Sci., 12, 2195-2199.

Lawn, B. R., Evans, A. G. and Marshall, D. B. (1980), J. Amer. Ceram. Soc., in press.

Marsh, D. M. (1964), Proc. Roy. Soc. A279, 420-435.

Marshall, D. B., Lawn, B. R. and Chantikul, P. (1979a), J. Mater. Sci., 14, 2225-2235.

Marshall, D. B. and Lawn, B. R. (1979b), J. Mater. Sci., 14, 2001-2012.

Marshall, D. B., Lawn, B. R. and Mecholsky, J. J. (1980), J. Amer. Ceram. Soc., 63, 358-360.

Mindlin, R. D. (1936), Physics, 7, 195-202.

Mulhearn, T. O. (1959), J. Mech. Phys. Solids, 7, 85-96.

Perrott, C. M. (1977), Wear, 45, 293-309.

Puttick, K. E., Smith, L. S. A., and Miller, L. E. (1977), J. Phys. D: Appl. Phys., 10, 617-632.

Rai, C. S. and Manghnani, M. H. (1976), J. Amer. Ceram. Soc., 59, 499-502.

Ruff, A. W. and Wiederhorn, S. M. (1979), "Treatise on Materials Science and Technology, Vol. 16, Erosion," Academic Press, 69-126.

Samuels, L. E. and Mulhearn, T. O. (1957), J. Mech. Phys. Solids, 5, 125-134.

Table I

Normalized Plastic Zone Size (β) and Material Properties

Materials	K_c $MPa\sqrt{m}$	H GPa	E GPa	β theory	β experiment
Soda lime glass[1]	.75	5.5	70	2.3	2.2[1]
Ge[2]	.5	9	140	2.5	
Al_2O_3+42V/o ZrO_2[3]	6.5	15	264	2.6	2.5[3]
ZrO_2(PSZ)[4]	6.9	11.4	170	2.6	
B_4C[4]	6.0	32.2	500	2.5	
Al_2O_3(s.c.)[5]	2.2	23	400	2.5	
Si(s.c.)[1]	.7	9	168	2.65	
SiC(h.p.)[4]	4.0	19.3	420	2.8	
Si_3N_4(h.p.)[4]	4.9	14.1	320	2.8	
MgO[6]	1.2	9.3	240[6a]	3.0	
MgF_2[6]	0.9	5.8	140[6b]	3.0	
Al_2O_3(h.p.)[6]	4.1	12	393[6c]	3.3	
ZnS[1]	1.0	1.9	103	4.0	3.0[1]
ZnS[7]	1.0	3.8[7a]	103	3.1	2.65[7a]
ZnSe[4]	.9	1.0	68	4.4	
Cold rolled steel[8]		3.4	200	4.6	4.5[8]
NaCl[6]	.4	.24	43[6a]	6.3	
Hot rolled brass[8]		.47	110	7.0	7.0[8]

(s.c.) = single crystal

(h.p.) = hot pressed

(1) Lawn, Evans and Marshall (1980)
(2) Lankford (1979)
(2a) Jaccodine (1963)
(3) Burlingame (1980)
(4) Evans (1979)
(5) Evans and Wilshaw (1976)
(6) Lawn and Evans (1977)
(6a) Lawn and Wilshaw (1975)
(6b) Rai and Manghnani (1976)
(6c) Freiman, Mickinney and Smith (1978)
(7) Dynamic Impact, estimated value
(7a) Computer simulated result, Evans (1979c)
(8) Mulhearn (1959)

Table II

RELATIVE THRESHOLD CHARACTERISTICS FOR

RADIAL, MEDIAN AND LATERAL CRACKS

Material	β	crack type	c^* (μm)	p^* (N)
Glass	2.2	R	1	0.4
		M	1	0.6
		L	3	2.0
SiC (Polycrystal)	2.8	R	3	5.0
		M	4	14
		L	7	40
Si_3N_4 (Polycrystal)	2.8	R	7	30
		M	12	80
		L	20	210
ZnS (Polycrystal)	4.0	R	20	8
		M	40	50
		L	65	100

Table III

RADIAL CRACK INITIATION THRESHOLD

Material	β	Prediction c^* (μm)	Prediction p^* (N)	Experimental Observations c^* (μm)	Experimental Observations p^* (N)
Glass	2.2	1.1	0.6	17	5 Δ
Ge(s.c.)	2.5	.16	.014	.25	.02 †
Si(s.c.)	2.65	.36	.05	.65	.03 †
Al_2O_3(s.c.)	2.5	.6	.4	3	.25-0.5 *†
NaCl(s.c.)	6.3	340	120	100	15-60 †
ZnS	4.0	17	8	70	6 ††

Δ Marshall and Lawn (1979b)

† Lankford and Davidson (1979)

†† Evans and Wilshaw (1976)

* Data obtained for a single grain (grain size 25μm)

Predictions and observations pertain to the unloading half-cycle for glass and to the loading half-cycle for all other materials.

Table IV

RADIAL FRACTURE PREDICTIONS FOR

POLYCRYSTALLINE MATERIALS

Material	β	K_c $MPam^{1/2}$	H GPa	E GPa	c^* (μm)	P^* (N)
B_4C	2.5	6.0	32.2	500	2	9
PSZ	2.6	6.9	11.4	170	20	240
SiC	2.8	4.0	19.3	420	3	5
Si_3N_4	2.8	4.9	14.1	320	7	30
MgF_2	3.0	.9	5.8	140	1.4	0.4
MgO	3.0	1.2	9.2	240	1	0.3
Al_2O_3	3.3	4.1	12.0	393	7	15
ZnSe	4.4	.9	1.0	68	50	3.4

FIGURE CAPTIONS

Fig. 1. The influence of indenter angle on the pyramidal hardness for three brittle materials: soda-lime glass, ZnS and As_2S_3 glass.

Fig. 2. The effect of the ratio of the modulus to the hardness, E/H, on the relative plastic zone size β (b/a) for a range of materials. Also shown are the theoretical predictions from the Hill solution, the Johnson analysis and the present analysis.

Fig. 3. The trend in the ratio of the indentation pressure to the yield strength with the modulus to yield strength ratio for a range of materials. Also shown are the predictions from the Hill solution, the Johnson analysis and the present analysis.

Fig. 4. A schematic showing the analytic procedure for creating a stress free surface and hence, for deforming the residual stress distribution: a) the general procedure, (b) the specific procedure for the hemispherical indentation and (c) the upper and lower bound conditions used for calculating the stress at peak load.

Fig. 5. The ratio of the hardness H to the spherical cavity pressure p around the hemispherical indentation interface for three values of the relative plastic zone size, β, indicating the relative uniformity of H/p.

Fig. 6. The ratio of the modified yield strength Y' to the spherical cavity pressure p around the hemispherical indentation interface for three values of the relative plastic zone size, β.

Fig. 7. Free surface correction factors m and m_r plotted as a function of the relative plastic zone size.

Fig. 8. The components of the peak load tangential stress at the surface (z=0) pertinent to radial fracture, indicating the initial cavity solution, the modification induced by the free surface and the point force solution used to compute the upper lower peak load stress.

Fig. 9. The tangential stress at the surface pertinent to radial fracture, obtained at both the peak load condition and in the residual condition, for two choices of the relative plastic zone size.

Fig. 10. The gradient in the near surface residual tangential stress, taken from the elastic/plastic boundary, surface intersection, for two choices of the relative plastic zone size.

Fig. 11. The tangential stress distribution pertinent to median cracks in the peak load (upper bound) and residual conditions.

Fig. 12. The gradient in the tensile stress component that dictates median fracture.

Fig. 13. The σ_{zz} stress that determines lateral fracture at different depth locations for a relative plastic zone size of 2.2 (a) at peak load and (b) the residual stress.

Fig. 14. The trends in the σ_{zz} stress with relative plastic zone size.

Fig. 15. A correlation of the predicted radial crack length with experimental data for well developed cracks.

Fig. 16. The variation of the predicted minimum threshold loads for radial and median cracking with the relative plastic zone size.

Fig. 17. The variation in the normalized stress intensity factor for radial cracks with the relative crack length.

Fig. 18. The coordinate system for stress analysis.

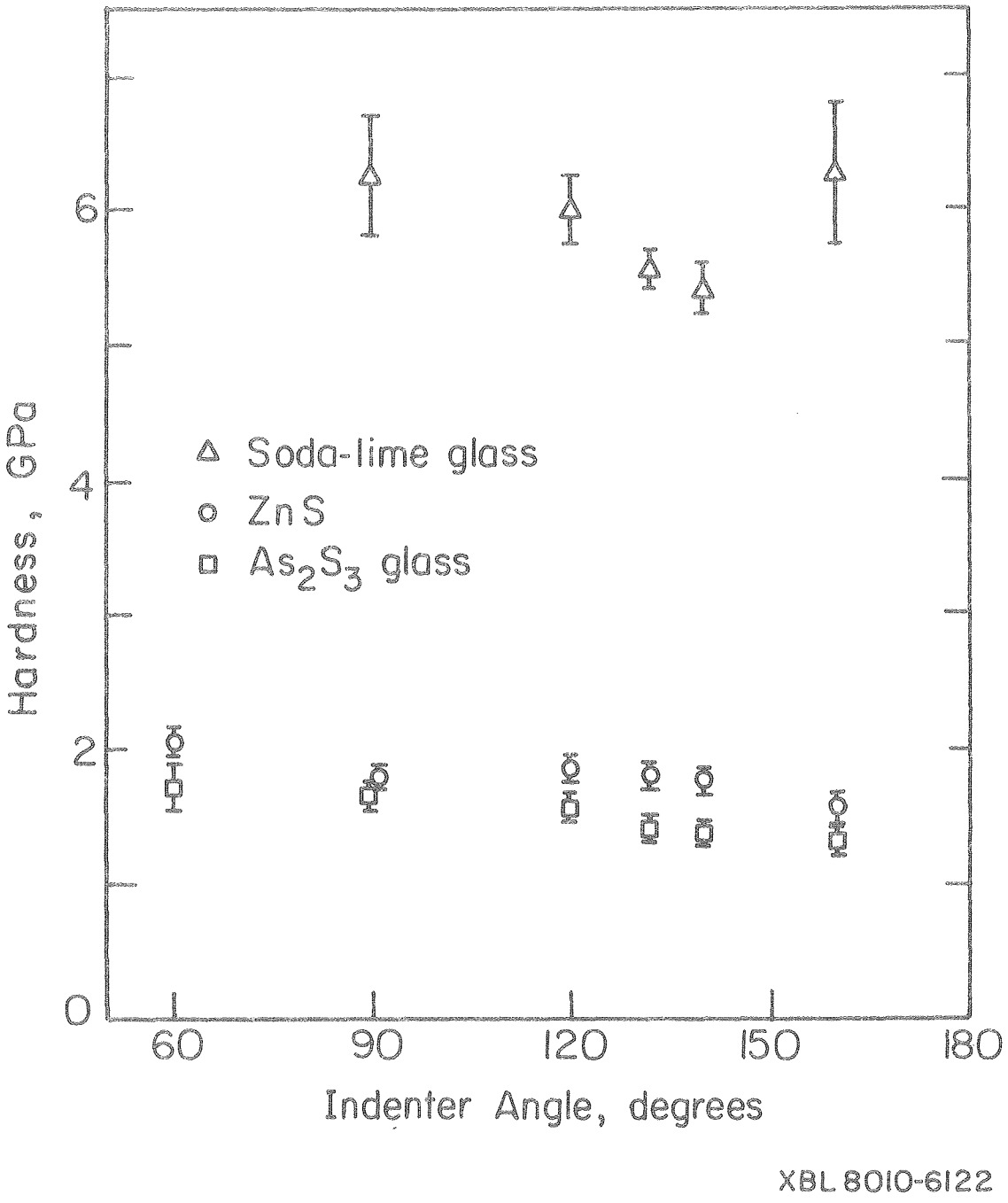
Hardness, GPa
0
2
4
6
60
90
120
150
180
Indenter Angle, degrees
Soda-lime glass
ZnS
As_2S_3 glass
XBL 8010-6122

Fig. 1

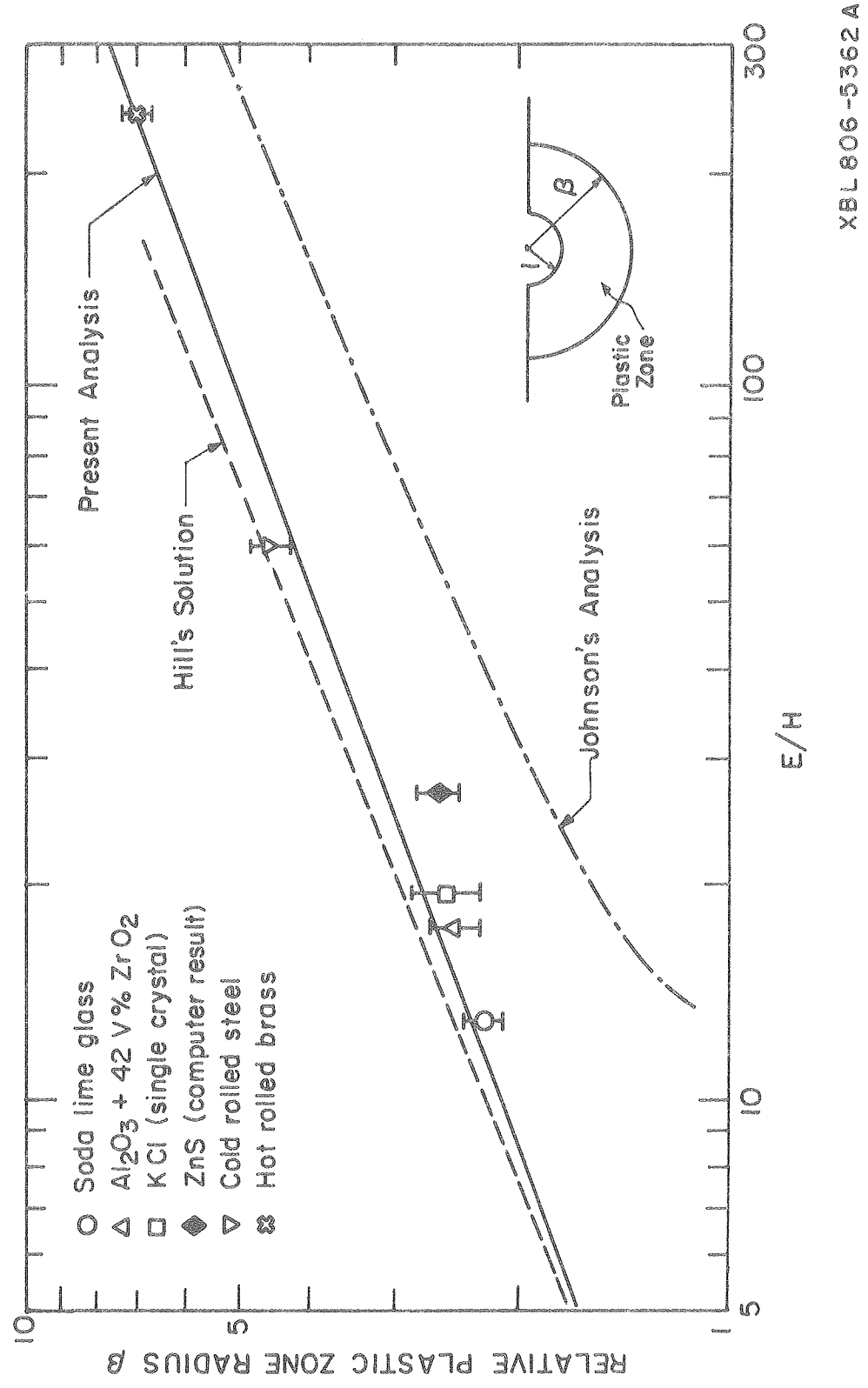

XBL806-5362A

Fig. 2

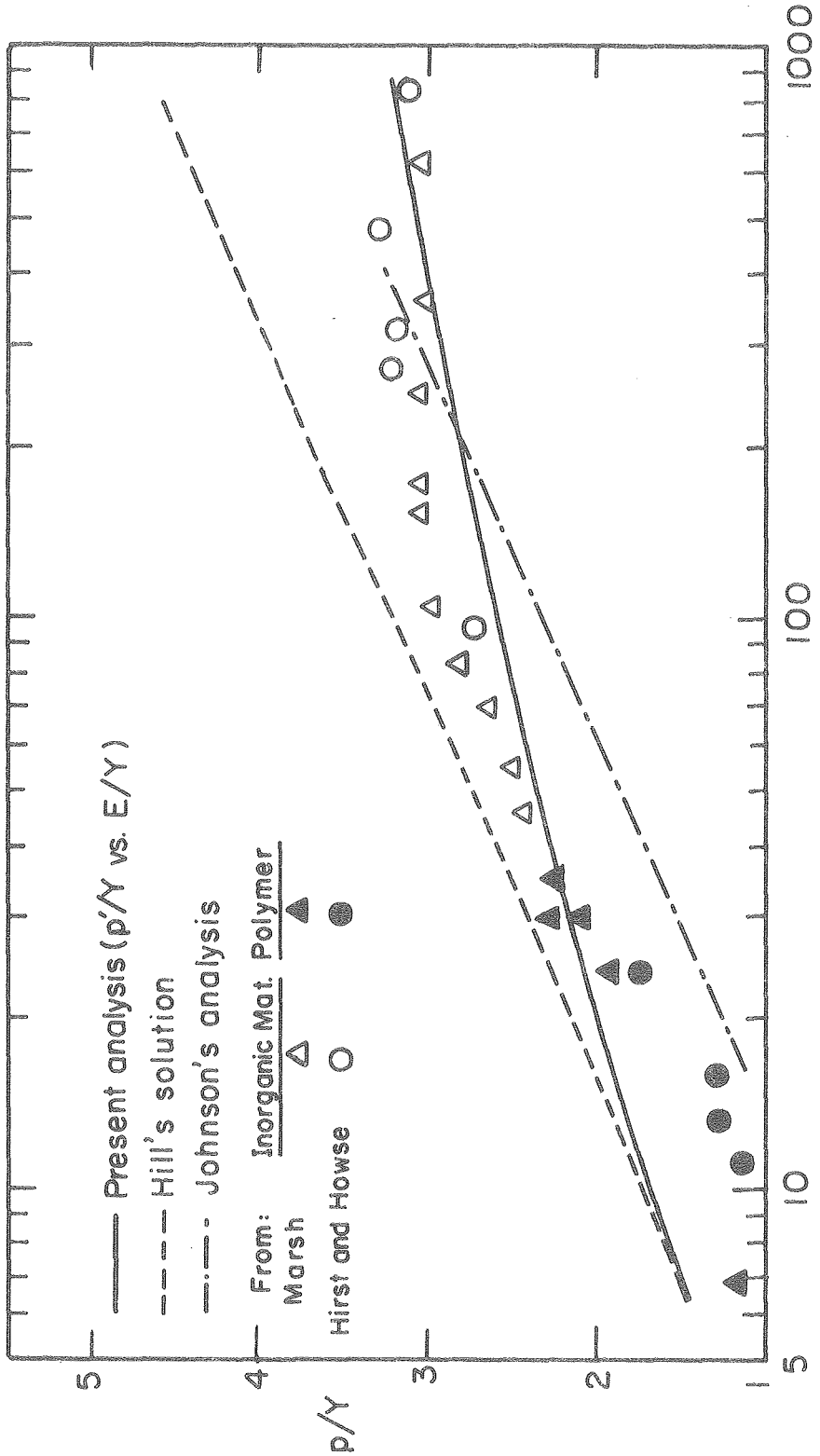

XBL806-5363

Fig. 3

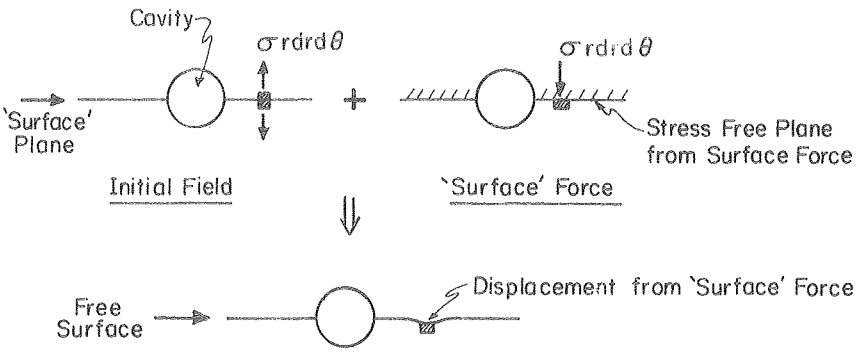

a) Elemental Procedure for Creating a Stress Free (Surface) Plane

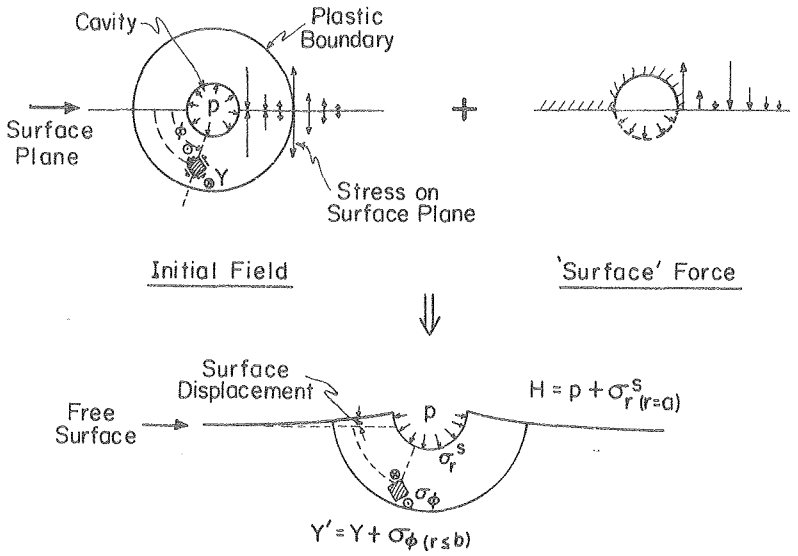

b) Specific Procedure

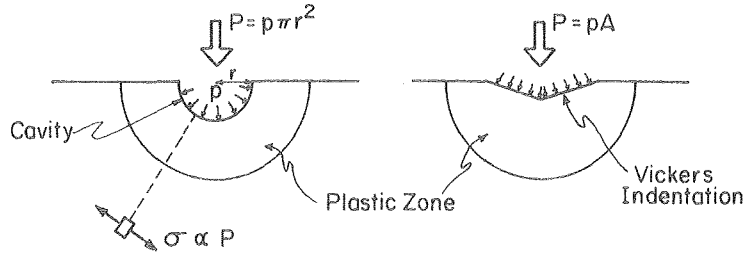

XBL806-5376

Fig. 4

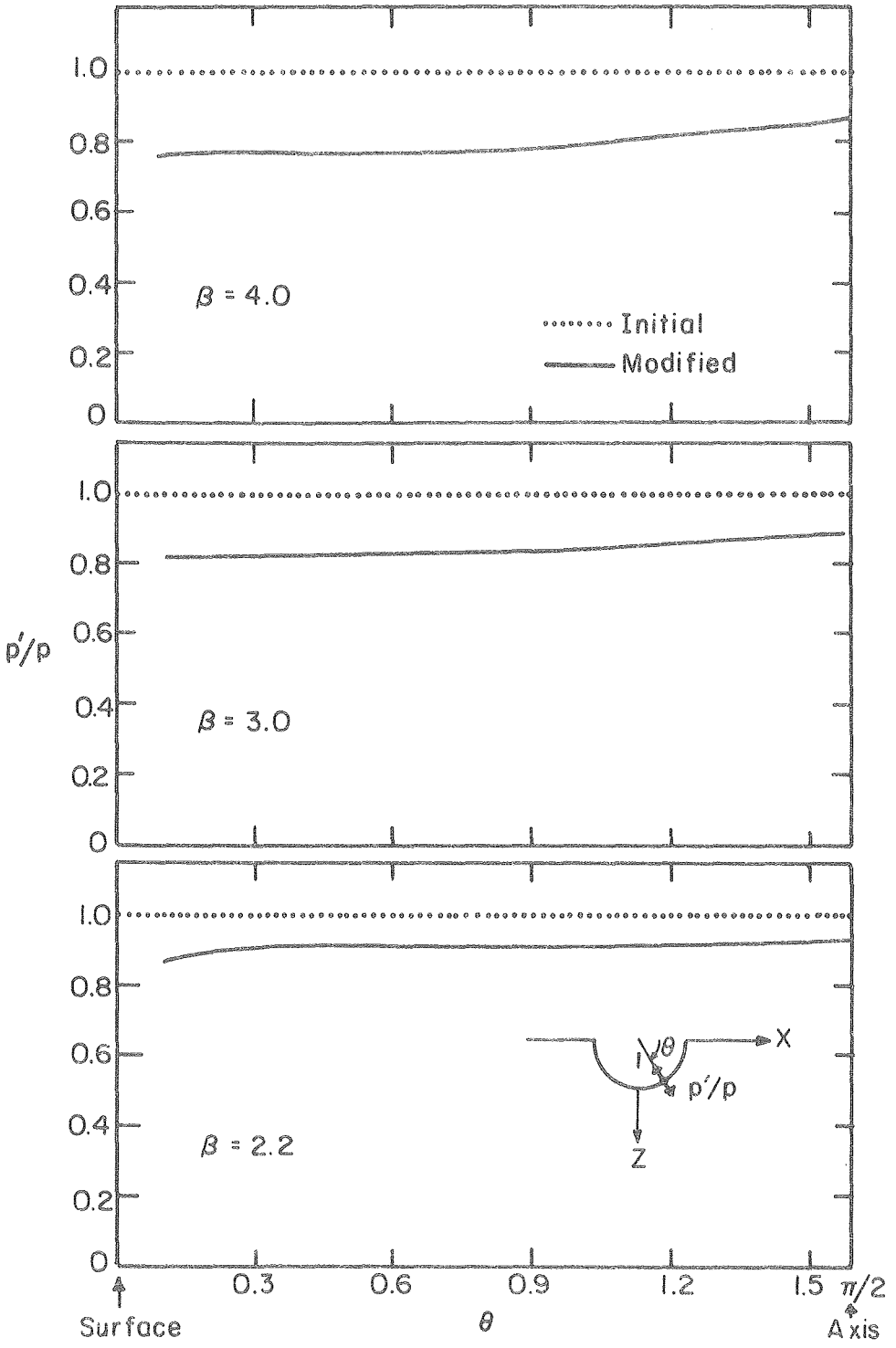

XBL 806-5365

Fig. 5

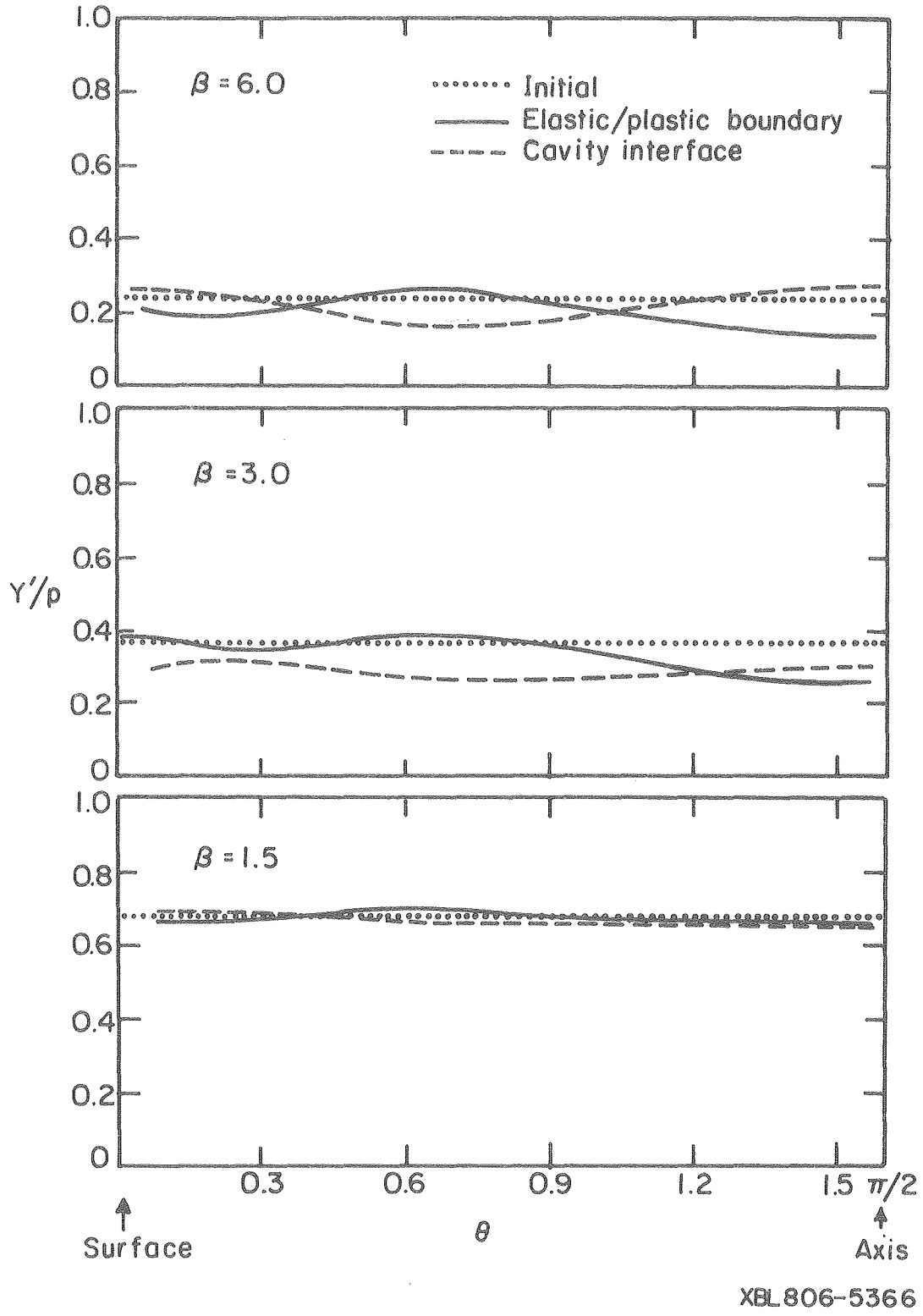
1.0
0.8
0.6
0.4
0.2
0
β = 6.0
Initial
Elastic/plastic boundary
Cavity interface
β = 3.0
β = 1.5
Y'/p
0.3
0.6
0.9
1.2
1.5
π/2
θ
Surface
Axis
XBL806-5366

Fig. 6

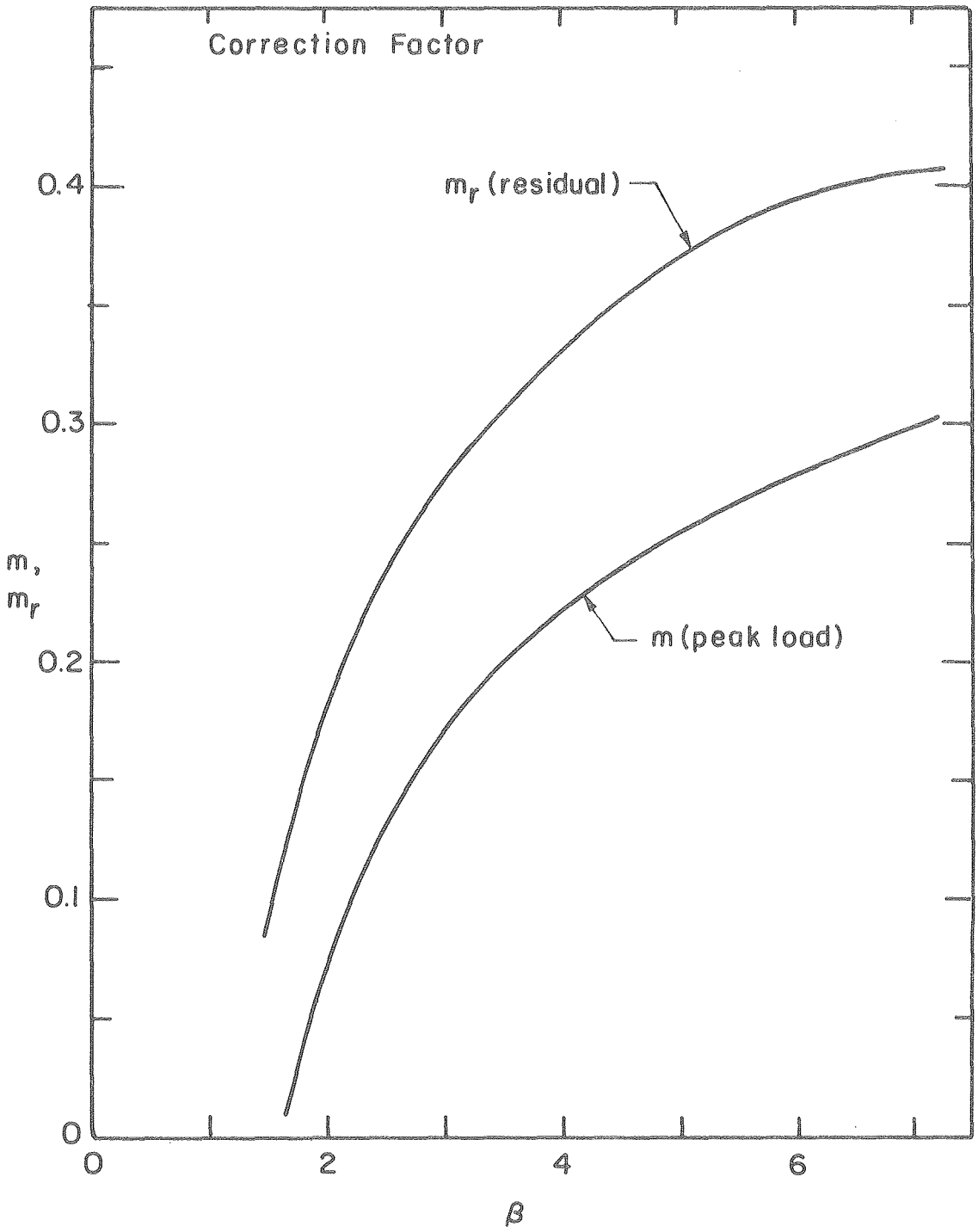
Correction Factor
m_r (residual)
m (peak load)
m, m_r
0.4
0.3
0.2
0.1
0
0
2
4
6
β
XBL 806-5364

Fig. 7

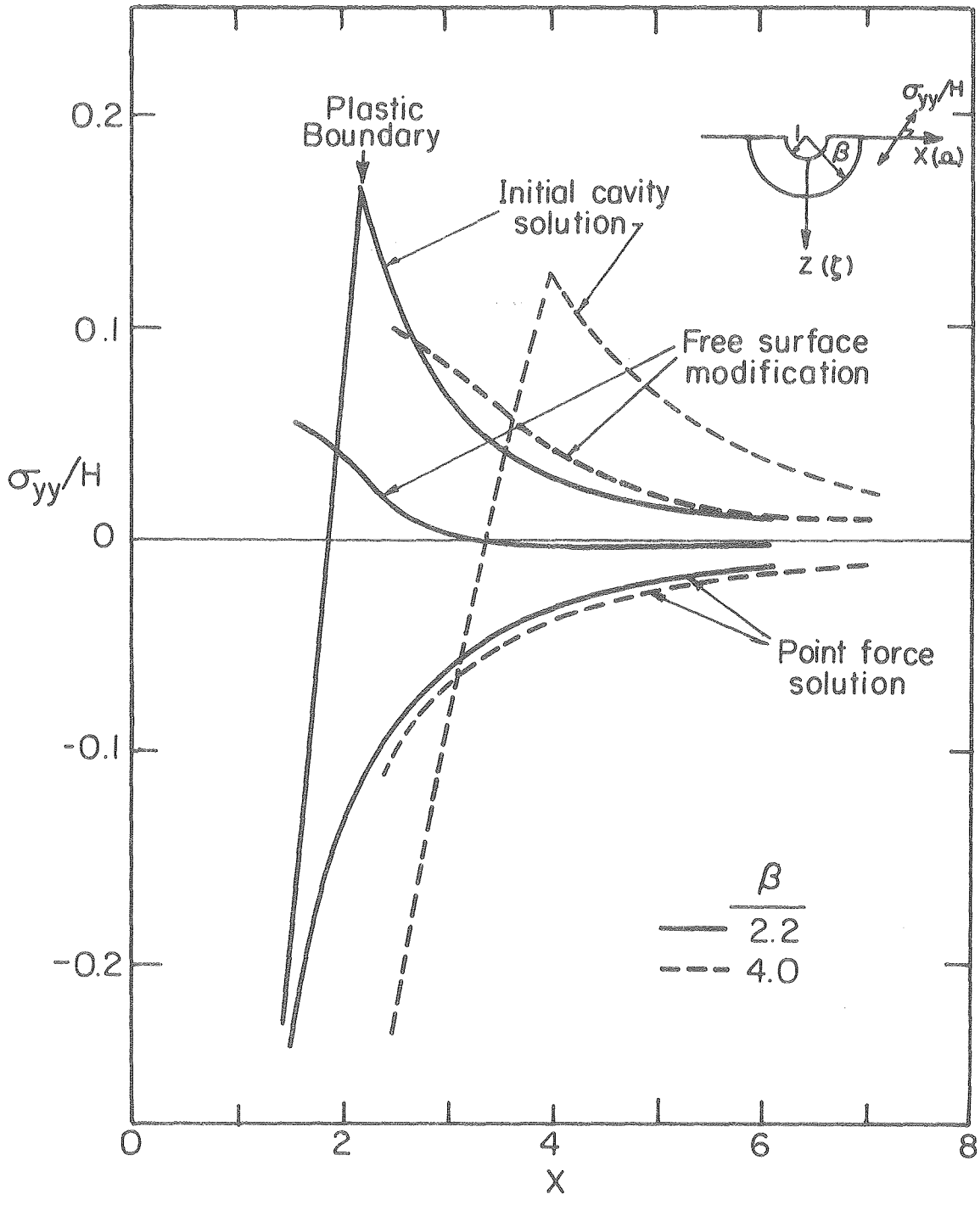

XBL 806-5372 A

Fig. 8

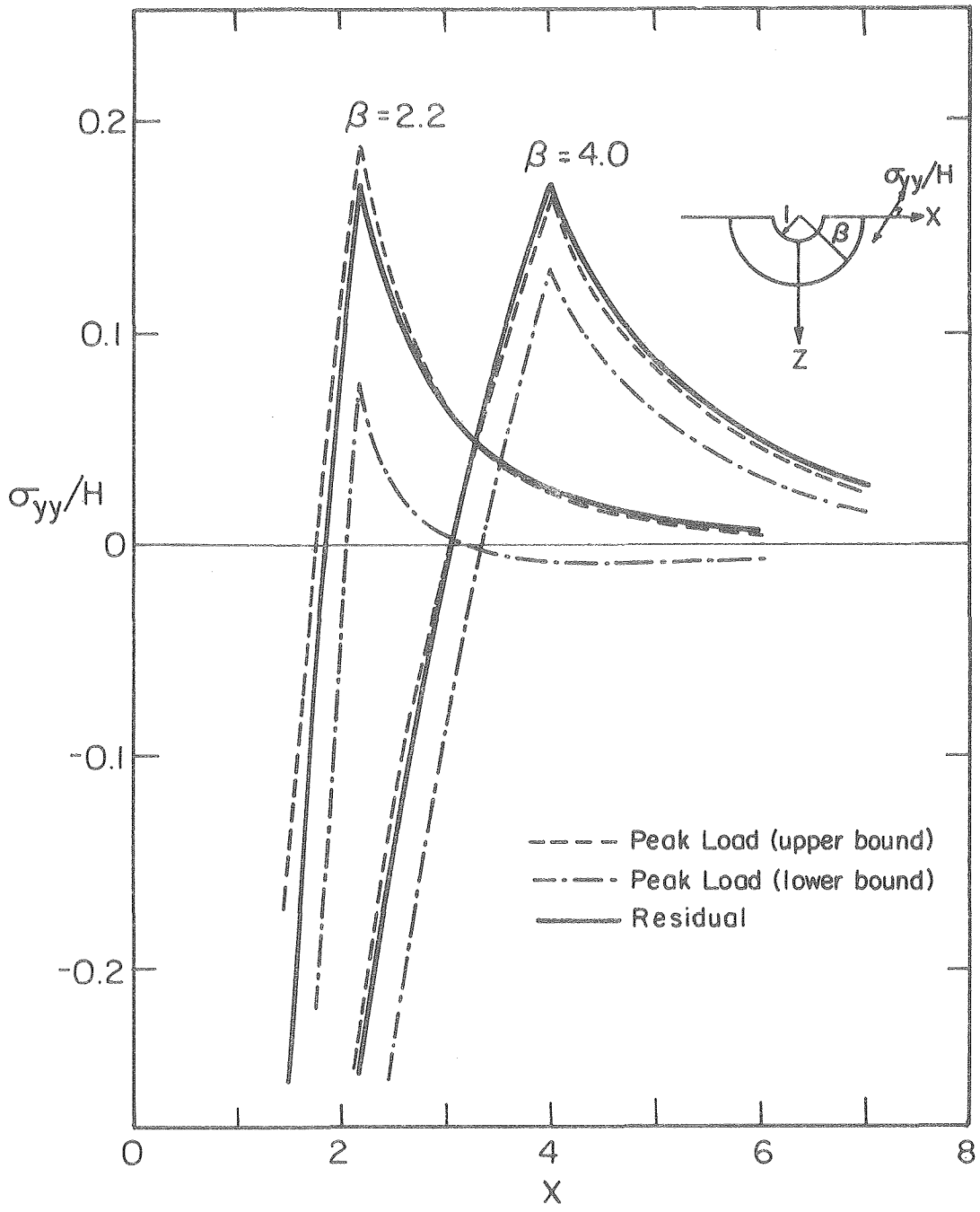

XBL 806-5371A

Fig. 9

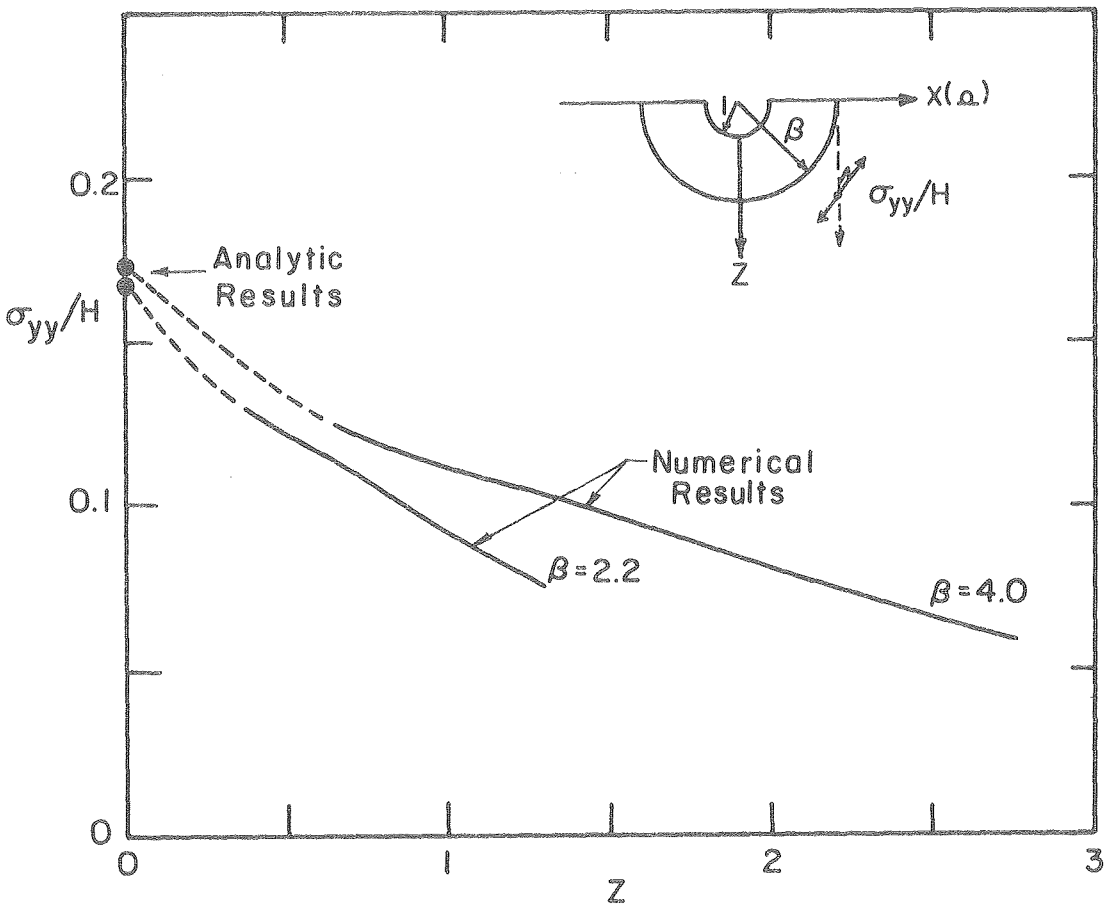

XBL806-5367A

Fig. 10

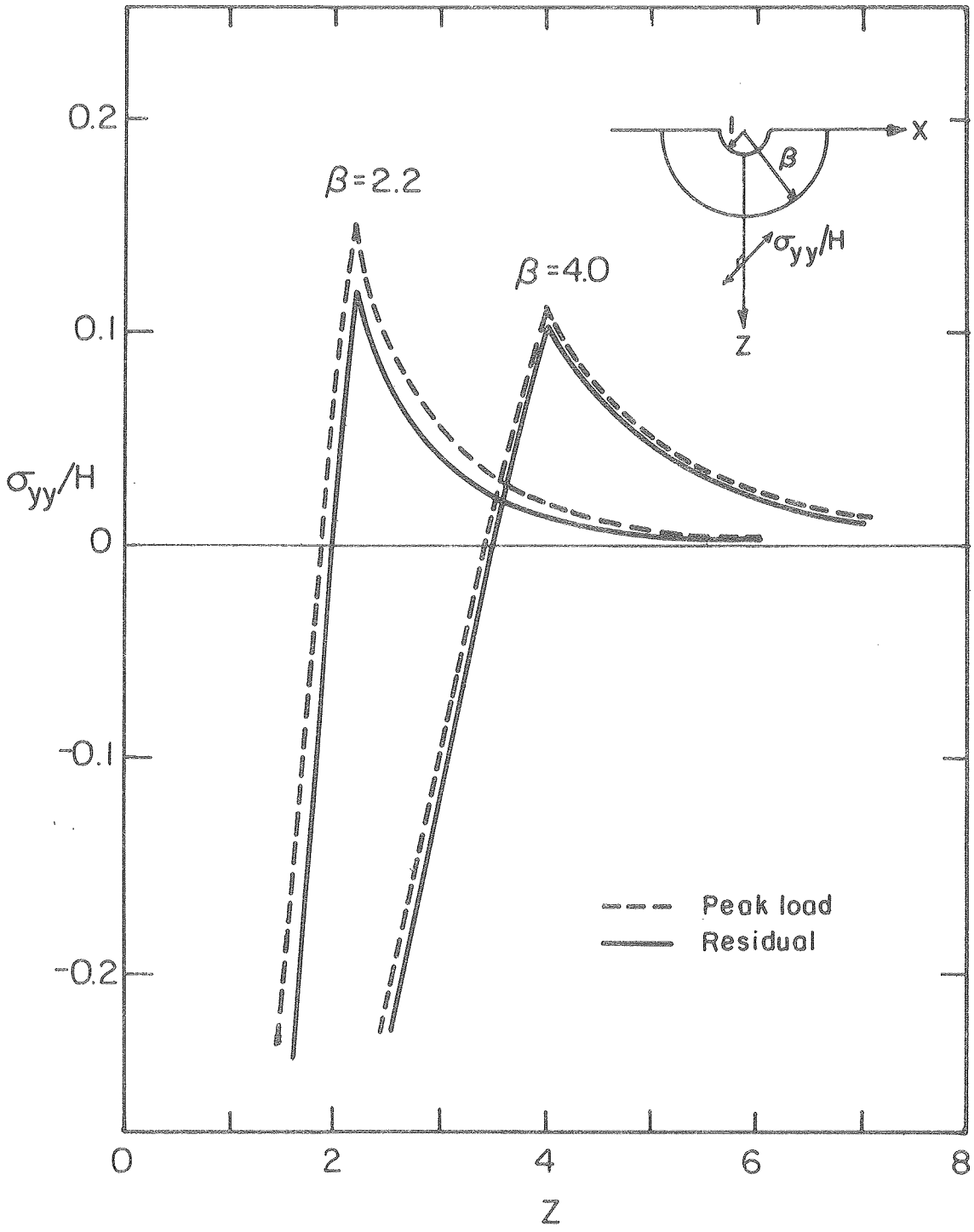
0.2
0.1
0
-0.1
-0.2
σ_{yy}/H
0
2
4
6
8
Z
β=2.2
β=4.0
X
Z
β
σ_{yy}/H
Peak load
Residual
XBL 806-5374 A

Fig. 11

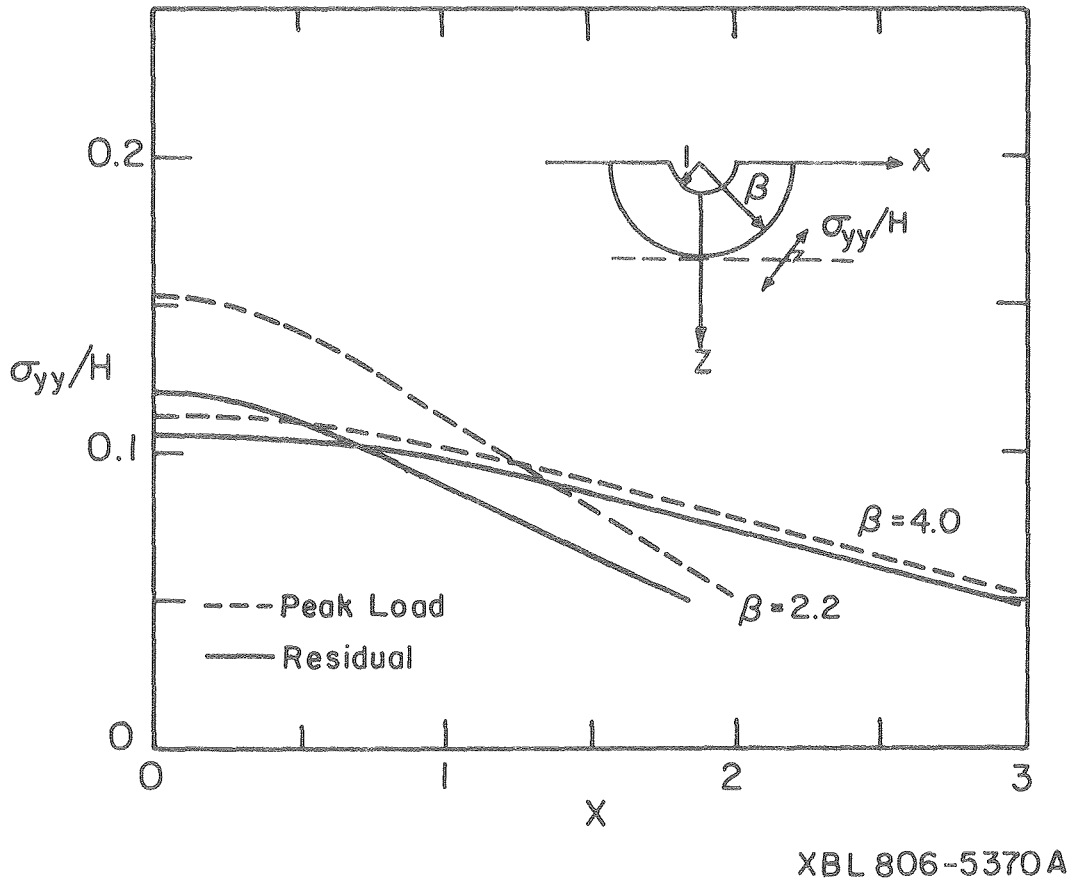
0.2
0.1
0
σ_{yy}/H
X
Z
β
σ_{yy}/H
$\beta = 4.0$
$\beta = 2.2$
Peak Load
Residual
0
1
2
3
X
XBL 806-5370A

Fig. 12

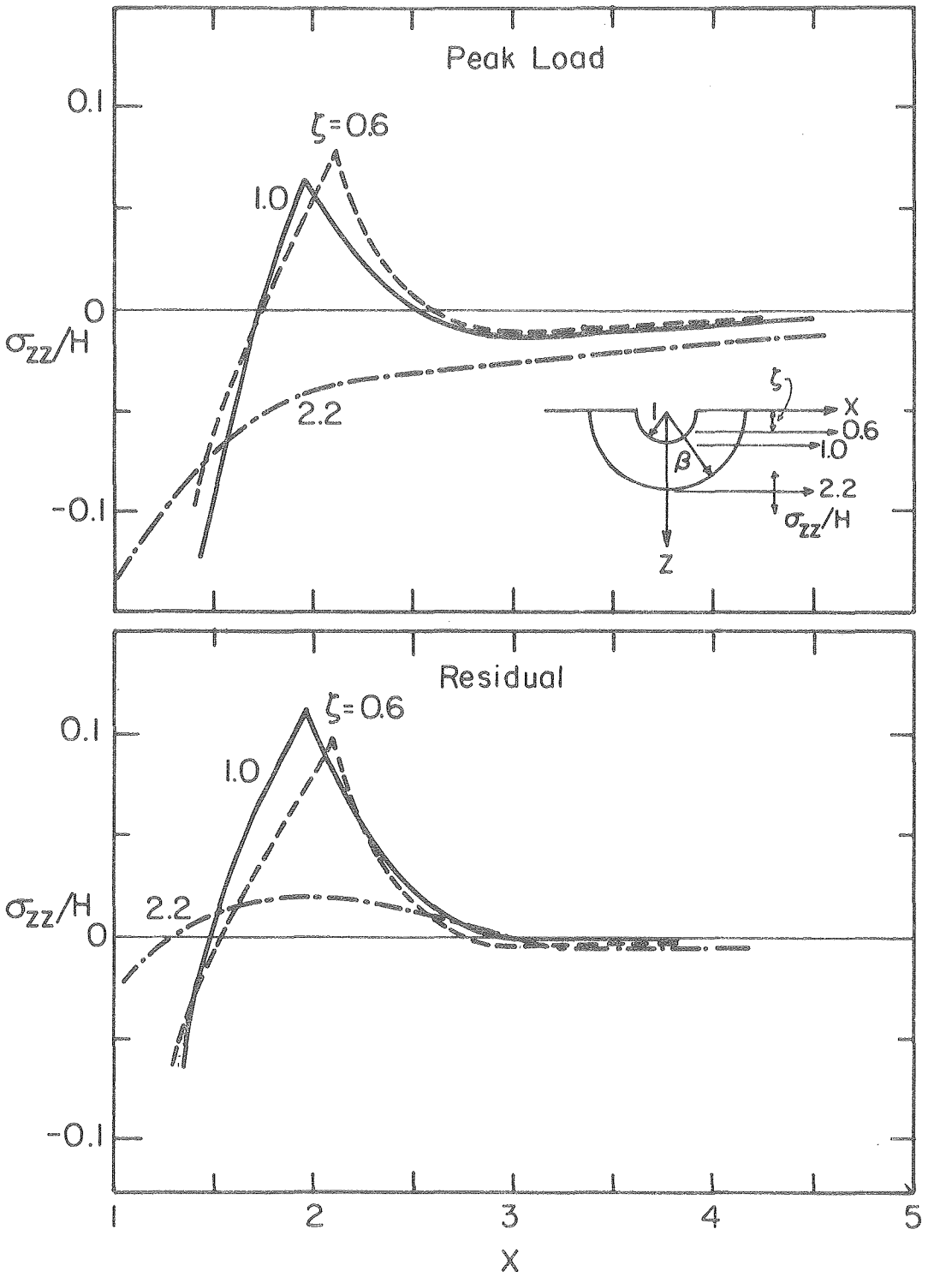

XBL 806-5373 A

Fig. 13

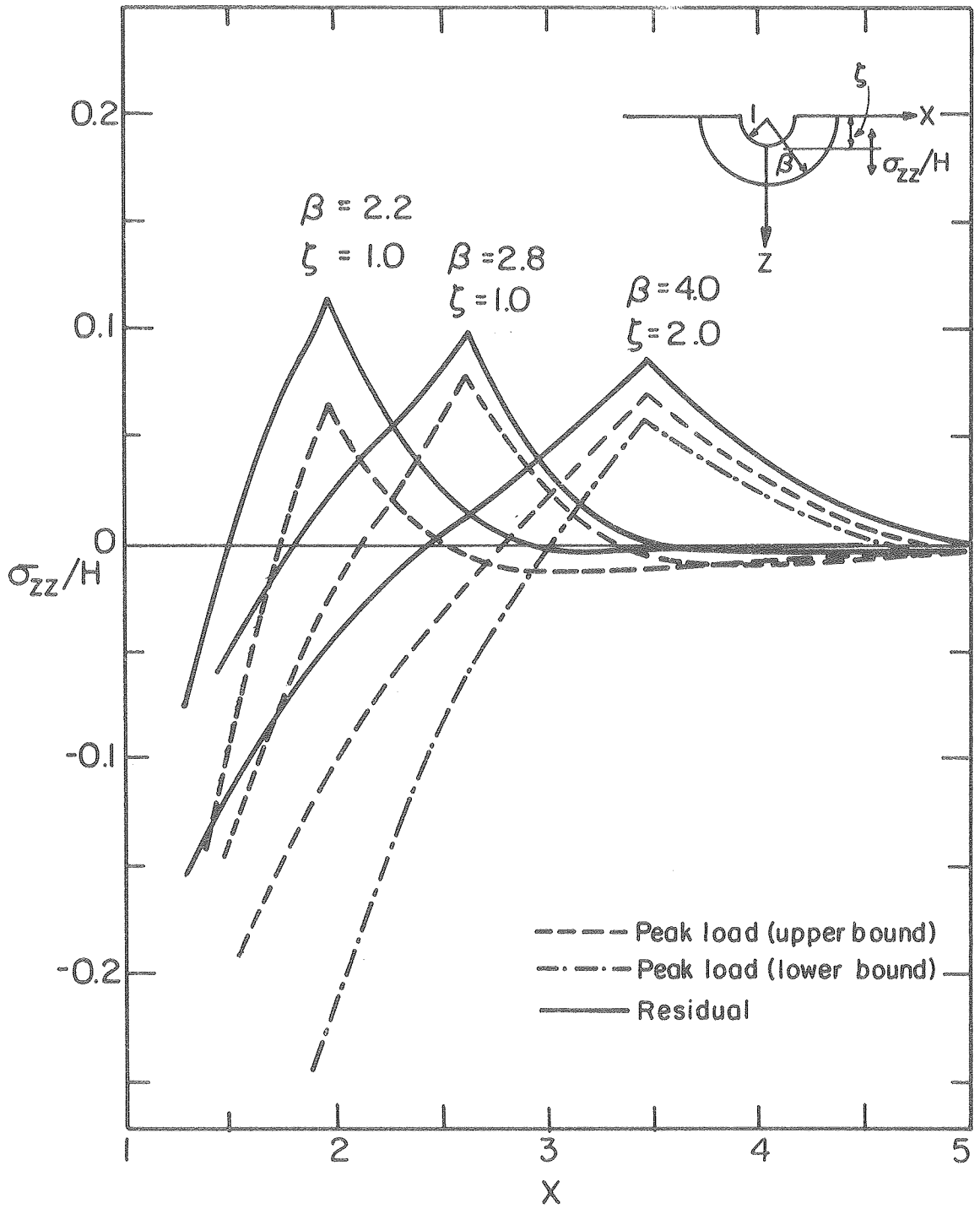

XBL 806-5375A

Fig. 14

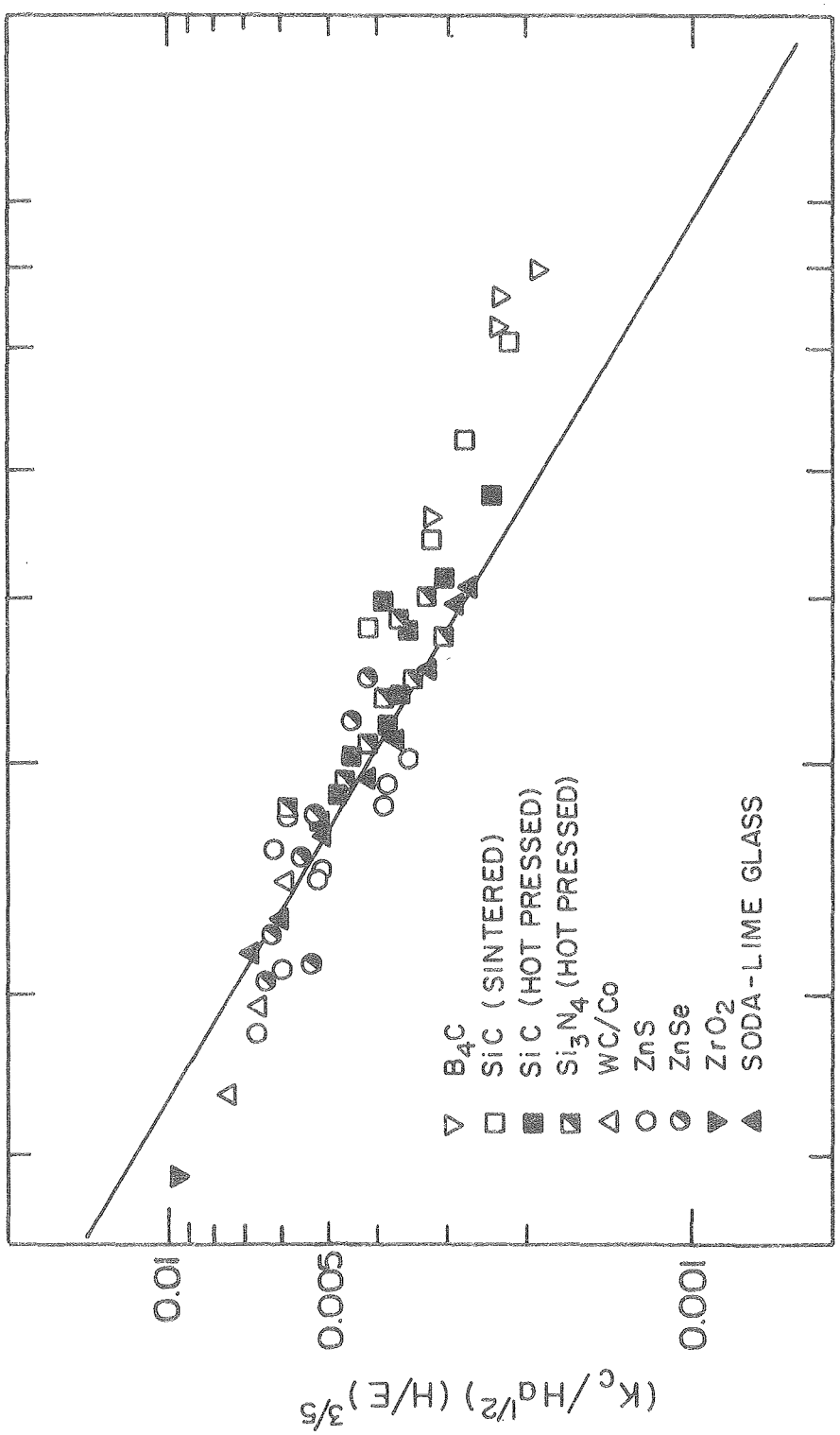
$(K_c/H_a^{1/2})(H/E)^{3/5}$
0.01
0.005
0.001
1.5
2
4
6
8
$c/\overline{a}$
B_4C
SiC (SINTERED)
SiC (HOT PRESSED)
Si_3N_4 (HOT PRESSED)
WC/Co
ZnS
ZnSe
ZrO_2
SODA-LIME GLASS
XBL8010-6081

Fig. 15

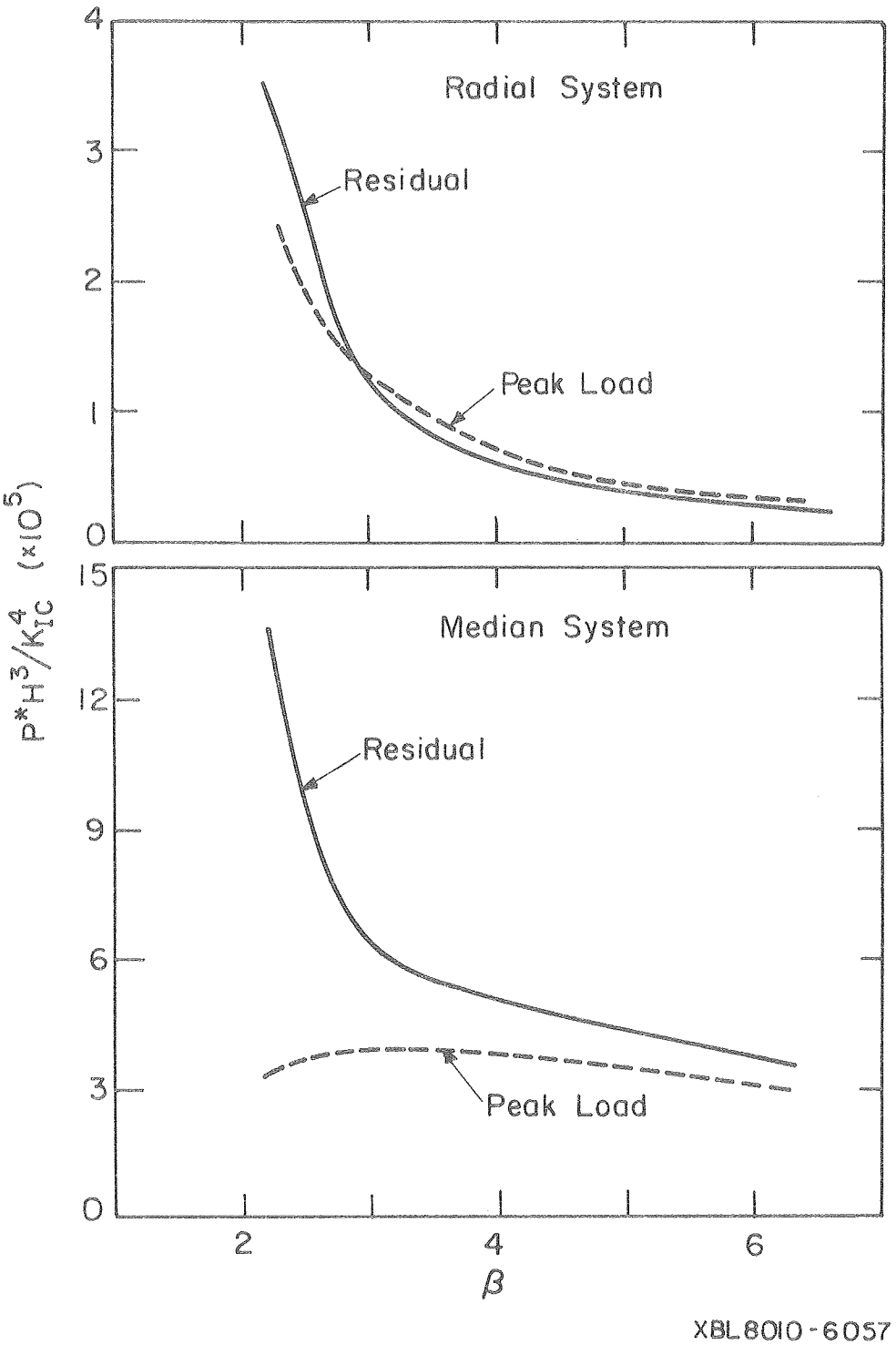
Radial System
Residual
Peak Load
Median System
Residual
Peak Load
P^*H^3/K_{IC}^4 ($\times 10^5$)
β
XBL8010-6057

Fig. 16

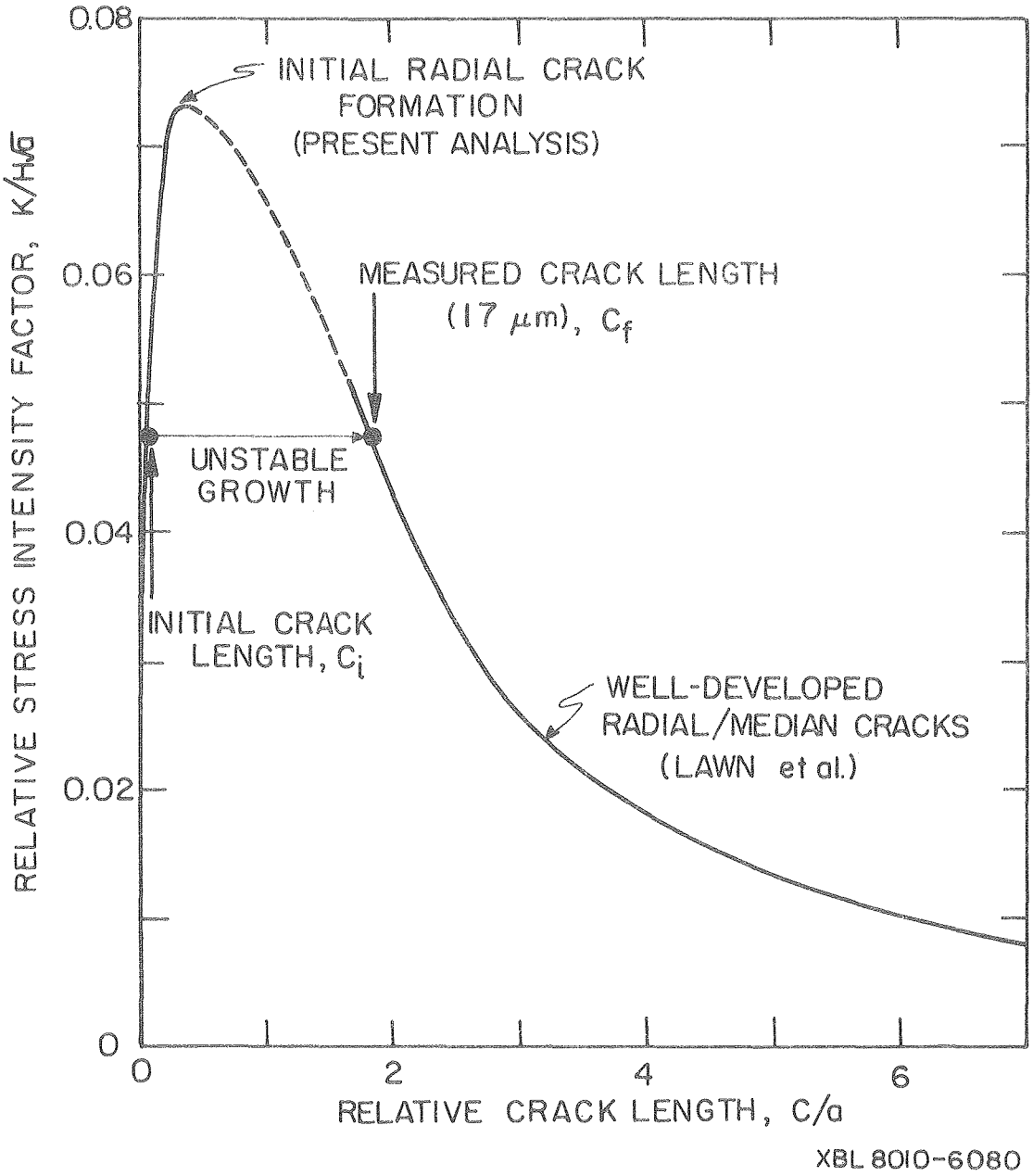
0.08
0.06
0.04
0.02
0
0
2
4
6
RELATIVE STRESS INTENSITY FACTOR, K/Hb
RELATIVE CRACK LENGTH, C/a
INITIAL RADIAL CRACK FORMATION (PRESENT ANALYSIS)
MEASURED CRACK LENGTH (17 μm), C_f
UNSTABLE GROWTH
INITIAL CRACK LENGTH, C_i
WELL-DEVELOPED RADIAL/MEDIAN CRACKS (LAWN et al.)
XBL 8010-6080

Fig. 17

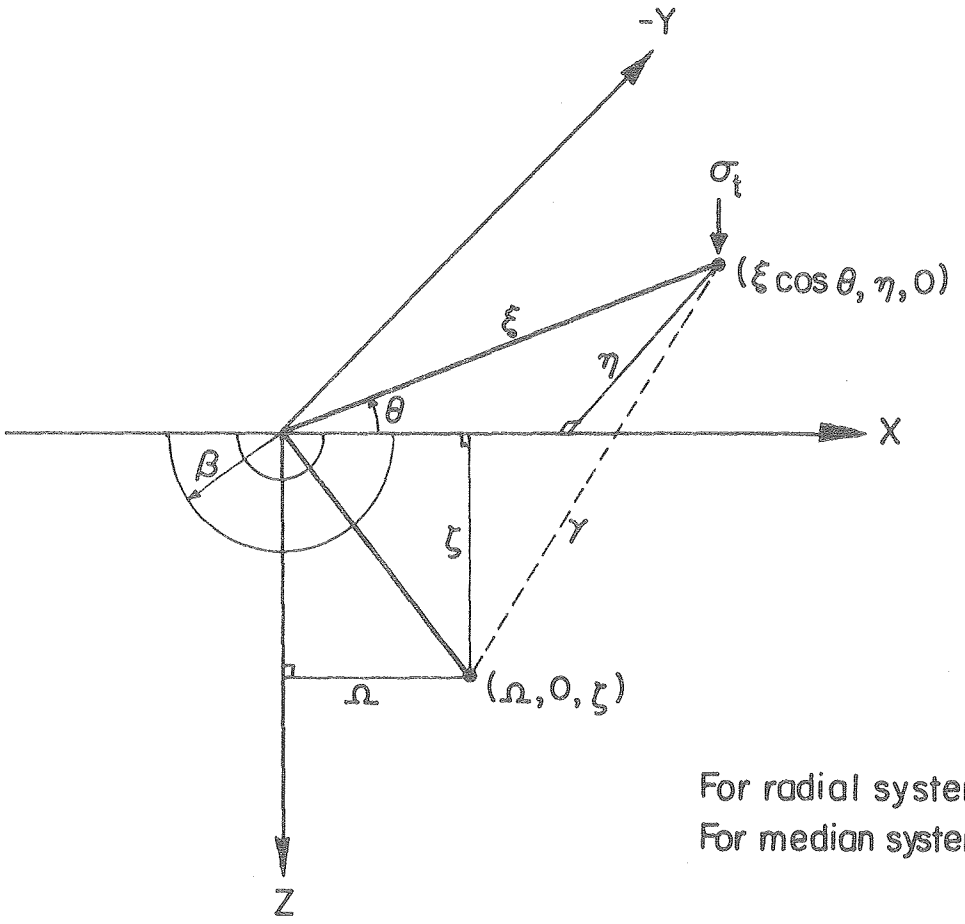

For radial system $\zeta = 0$
For median system $\Omega = 0$

XBL8010-6056

Fig. 18